Novel *DNM1L* variants impair mitochondrial dynamics through divergent mechanisms

Kelsey A. Nolden[1*], John M. Egner[1*], Jack J. Collier[2,3], Oliver M. Russell[2], Charlotte L. Alston[2,4], Megan C. Harwig[1], Michael E. Widlansky[5], Souphatta Sasorith[6], Inês A. Barbosa[7], Andrew G. L. Douglas[8,9], Julia Baptista[10,11], Mark Walker[12], Deirdre E. Donnelly[13], Andrew A. Morris[14], Hui Jeen Tan[15], Manju A. Kurian[16], Kathleen Gorman[17,18], Santosh Mordekar[19], Charu Deshpande[20], Rajib Samanta[21], Robert McFarland[2,4], R. Blake Hill[1], Robert W. Taylor[2,4] and Monika Oláhová[2]

[1] Department of Biochemistry, Medical College of Wisconsin, Milwaukee, USA

[2] Wellcome Centre for Mitochondrial Research, Newcastle University, Translational and Clinical Research Institute, Faculty of Medical Sciences, Newcastle upon Tyne, UK

[3] Department of Neurology and Neurosurgery, Montreal Neurological Institute, McGill University, Montreal, Canada

[4] NHS Highly Specialised Service for Rare Mitochondrial Disorders, Newcastle upon Tyne Hospitals NHS Foundation Trust, Newcastle upon Tyne, UK

[5] Department of Medicine, Division of Cardiovascular Medicine and Department of Pharmacology, Medical College of Wisconsin, Milwaukee, Wisconsin, USA

[6] Laboratoire de Génétique Moléculaire, Centre Hospitalier Universitaire and PhyMedExp, INSERM U1046, CNRS UMR 9214, Montpellier, France

[7] Department of Medical and Molecular Genetics, School of Basic & Medical Biosciences, King's College London, UK

[8] Wessex Clinical Genetics Service, University Hospital Southampton NHS Foundation Trust, Southampton, UK

[9] Human Development and Health, Faculty of Medicine, University of Southampton, Southampton, UK

[10] Exeter Genomics Laboratory, Royal Devon & Exeter NHS Foundation Trust, Exeter, UK

[11] Institute of Biomedical and Clinical Science, University of Exeter Medical School, Exeter, UK

[12] Department of Cellular Pathology, University Hospital Southampton NHS Foundation Trust, Southampton, UK

[13] Northern Ireland Regional Genetics Centre, Belfast Health and Social Care Trust, Belfast City Hospital, Belfast, Northern Ireland, UK

[14] Willink Metabolic Unit, Manchester Centre for Genomic Medicine, Manchester University Hospitals NHS Foundation Trust, Manchester, UK

[15] Department of Paediatric Neurology, Royal Manchester Children's Hospital, Manchester University Hospitals NHS Foundation Trust, Manchester, UK

[16] Developmental Neurosciences Department, Zayed Centre for Research into Rare Diseases in Children, UCL GOS Institute of Child Health, Faculty of Population Health Sciences, London, UK

[17] Department of Neurology and Clinical Neurophysiology, Children's Health Ireland at Temple Street, Dublin, Ireland

[18] School of Medicine and Medical Science, University College Dublin, Dublin, Ireland

[19] Department of Paediatric Neurology, Sheffield Children's Hospital, Sheffield, UK

[20] Clinical Genetics Unit, Guys and St. Thomas' NHS Foundation Trust, London, UK

[21] University Hospitals Leicester NHS Trust, Department of Paediatric Neurology, Leicester, UK

* These authors contributed equally

Correspondence should be addressed to:

Monika Oláhová (monika.olahova@ncl.ac.uk)

Abstract

Imbalances in mitochondrial and peroxisomal dynamics are associated with a spectrum of human neurological disorders. Mitochondrial and peroxisomal fission both involve Dynamin-related Protein 1 (DRP1) oligomerisation and membrane constriction, although the precise biophysical mechanisms by which distinct DRP1 variants affect the assembly and activity of different DRP1 domains remains largely unexplored. We analysed four unreported *de novo* heterozygous variants in the Dynamin-1-Like gene *DNM1L*, affecting different highly conserved DRP1 domains, leading to developmental delay, seizures, hypotonia and/or rare cardiac complications in infancy. Single nucleotide DRP1 stalk domain variants were found to correlate with more severe clinical phenotypes, with *in vitro* recombinant human DRP1 mutants demonstrating greater impairments in protein oligomerisation, DRP1-peroxisomal recruitment and both mitochondrial and peroxisomal hyperfusion compared to GTPase or GTPase-effector domain variants. Importantly, we identified a novel mechanism of pathogenesis, where a p.Arg710Gly variant uncouples DRP1 assembly from assembly-stimulated GTP hydrolysis, providing mechanistic insight into how assembly state information is transmitted to the GTPase domain. Together, these data reveal that discrete, pathological *DNM1L* variants impair mitochondrial network maintenance by divergent mechanisms.

Keywords

DNM1L; GTPase activity, mitochondrial fission, peroxisomal fission, mitochondrial disease; *de novo* dominant disease mechanism

Introduction

In response to various environmental and cellular stimuli, the mitochondrial network undergoes continues architectural remodelling. The morphology of the mitochondrial network is controlled by two dynamic events – mitochondrial fission and fusion (Touvier *et al*, 2015; Dorn *et al*, 2015; Harvey, 2019; Roy *et al*, 2015; Kasahara & Scorrano, 2014; Wai & Langer, 2016; Mishra & Chan, 2014). The balance of these events is essential for even distribution of mitochondrial content, mitochondrial protein quality control and regulation of mitochondrial activity. Besides regulating mitochondrial metabolism, mitochondrial fission and fusion events play an essential role in a number of cellular processes, including cell cycle regulation (Horbay & Bilyy, 2016; Qian *et al*, 2012; Pangou & Sumara, 2021), immune response (Cervantes-Silva *et al*, 2021) and cell death (Aouacheria *et al*, 2017).

Mitochondrial fusion is largely mediated by the outer mitochondrial membrane proteins Mitofusin 1 (MFN1) and Mitofusin 2 (MFN2) and the inner mitochondrial membrane protein Optic Atrophy 1 (OPA1). Perturbed mitochondrial fusion leads to morphological changes characterised by the presence of fragmented mitochondria. Conversely, mitochondrial fission leads to the division of mitochondria and impairment of this process causes the formation of hyperfused mitochondrial networks (Dorn, 2019; Tilokani *et al*, 2018; Collier & Taylor, 2021).

The GTPase Dynamin-1-Like protein (also referred to as Dynamin Related Protein 1 or DRP1), encoded by the *DNM1L* gene, is the central effector of mitochondrial division. DRP1 is predominantly found in the cytosol, but upon activation is recruited to the outer mitochondrial surface by membrane anchored receptor proteins - including mitochondrial fission factor (MFF), mitochondrial fission protein 1 (FIS1) and the mitochondrial dynamics proteins (MID49 and MID51) (Yoon *et al*, 2003; Ihenacho *et al*, 2021; Smirnova *et al*, 2001; Otera *et al*, 2010; Gandre-Babbe & Van Der Bliek, 2008; James *et al*, 2003; Losón *et al*, 2013; Palmer *et al*, 2011; Liu *et al*, 2013; Stojanovski *et al*, 2004) - to mediate mitochondrial fission. DRP1 assembles at mitochondria-endoplasmic reticulum (ER) contact sites (Friedman *et al*, 2011), organising into higher-order oligomeric complexes that encompass mitochondrial tubules in a circumferential manner in either a helical (Kalia *et al*, 2018; Fröhlich *et al*, 2013; Mears *et al*, 2011) or filamentous organization (Kalia *et al*, 2018). Subsequent GTP binding and hydrolysis drives conformational changes in oligomeric DRP1 structures, resulting in constriction of the membrane diameter, before a concert of

interactions between mitochondria, other organelles and vesicles trigger scission (Kalia *et al*, 2018; Koirala *et al*, 2013; Mears *et al*, 2011; Kraus & Ryan, 2017; Basu *et al*, 2017; Nagashima *et al*, 2020). Peroxisomal fission is independent of mitochondrial fission but requires many components of the mitochondrial fission apparatus, including DRP1, MFF and FIS1 (Otera *et al*, 2010; Yamano *et al*, 2014; Koch & Brocard, 2012; Li & Gould, 2003; Koch *et al*, 2005; Kobayashi *et al*, 2007; Gandre-Babbe & Van Der Bliek, 2008).

The importance of mitochondrial division and dynamics is evidenced by the fact that *Dnm1l*$^{-/-}$ knockout mice are embryonic lethal (Wakabayashi *et al*, 2009; Ishihara *et al*, 2009). Furthermore, cardiac-specific (Ishihara *et al*, 2015; Song *et al*, 2015; Ashrafian *et al*, 2010; Ikeda *et al*, 2015) and brain-specific (Wakabayashi *et al*, 2009; Ishihara *et al*, 2009) ablation of DRP1 leads to lethal dilated cardiomyopathy and defective cerebellar development with early postnatal death, respectively. Defects in human mitochondrial dynamics caused by *de novo* monoallelic or bi-allelic pathogenic *DNM1L* variants are often associated with developmental delay, hypotonia and neurological disorders, including encephalopathy, refractory seizures and/or autosomal dominant optic atrophy (**Table S1**). It has been suggested that *de novo* heterozygous *DNM1L* variants likely exert a dominant-negative effect over the wild type allele, impairing its ability to effectively achieve mitochondrial division (Whitley *et al*, 2018). However, the biophysical basis of impaired mitochondrial dynamics underpinned by human *DNM1L* variants remain unresolved. The first reported pathogenic *DNM1L* (NM_ 012062.5) variant, c.1184C>A, p.Ala395Asp (Waterham *et al*, 2007), located in the stalk domain of DRP1, impairs DRP1 higher-order assembly and GTPase activity (Chang *et al*, 2010), but whether alternative molecular mechanisms drive mitochondrial hyperfusion and pathology caused by other pathological *DNM1L* variants, particularly affecting different domains, remains unknown.

Mitochondrial disease can arise from *de novo* heterozygous (Whitley *et al*, 2018; Vanstone *et al*, 2016; Longo *et al*, 2020; Wei & Qian, 2021; Verrigni *et al*, 2019; Chao *et al*, 2016; Sheffer *et al*, 2016; Gerber *et al*, 2017; Chang *et al*, 2010; Waterham *et al*, 2007; Zaha *et al*, 2016; Vandeleur *et al*, 2019; Batzir *et al*, 2019; Fahrner *et al*, 2016; Liu *et al*, 2021), bi-allelic compound heterozygous (Nasca *et al*, 2016; Yoon *et al*, 2016; Hogarth *et al*, 2018; Verrigni *et al*, 2019) and homozygous recessive (Hogarth *et al*, 2018) *DNM1L* variants (**Table S1**). The clinical course of individuals harbouring *de novo DNM1L* variants are both variable and unpredictable. Although there are no clear parallels between the clinical presentations and location of reported *DNM1L* mutations, some patterns in genotype-phenotype correlations are starting to emerge. Over time, we anticipate that an increased

mechanistic understanding of how *DNM1L* variants cause mitochondrial hyperfusion will enable us to understand whether specific variants may be amenable to therapeutic intervention.

Using massively parallel sequencing techniques, we identified five unrelated patients harbouring four previously unreported *de novo* heterozygous variants in *DNM1L*. Patients presented with a spectrum of neurological symptoms, as well as rarely reported cardiomyopathy, a clinical feature recapitulated in cardiac-specific *Dnm1l*$^{-/-}$ knockout mice (Ikeda *et al*, 2015). Extensive *in vivo* and *in vitro* functional characterisation of patient *DNM1L* variants demonstrate that they impair mitochondrial network maintenance and peroxisomal morphology *via* divergent mechanisms, with variants in the DRP1 stalk domain correlating to greater disease severity and earlier age of death. We found that distinct *DNM1L* variants either increased or diminished GTPase activity, altered protein stability and impaired oligomerisation in the aetiology of *DNM1L*-related mitochondrial disease, subsequently leading to impaired mitochondrial and peroxisomal recruitment with subsequent organellar hyperfusion and functional deficiencies. In addition, we show that the p.Arg710Gly DRP1 GTPase effector domain (GED) variant can impair assembly driven GTP hydrolysis through disruption of the highly conserved hinge 1 region in a human dynamin related protein. Uniquely, this variant uncouples DRP1 oligomerisation from assembly-stimulated GTP hydrolysis, giving us a powerful tool to investigate how signals are transmitted from assembly state to the GTPase domain in dynamin-related proteins.

Results

Clinical data

We identified five individuals (patient 1 (P1), patient 2 (P2), patient 3 (P3), patient 4 (P4) and patient 5 (P5)) from five unrelated non-consanguineous families (**Fig 1A)** with developmental delay (four patients), a broad range of neurological manifestations including epilepsy (three patients), hypotonia (two patients) and/or cardiac problems (two patients). The detailed clinical findings of all five patients are described in the **Supplementary information** and **Table 1**.

Molecular genetics investigations identify novel *de novo* heterozygous variants in *DNM1L*

To uncover candidate disease causing variants in P1-P5, we utilised massively parallel sequencing techniques. Mitochondrial DNA (mtDNA) genome sequencing of blood-

derived DNA from P1 did not identify any likely pathogenic variants whilst mtDNA copy number analysis using muscle-derived DNA found no evidence of mtDNA depletion. Trio array comparative genomic hybridization (aCGH) revealed a 15-20 kb chromosome 17p13.3 microdeletion of uncertain significance within an intronic region of YWHAE but this was shown to be inherited from the father. Diagnostic whole exome sequencing (WES) analysis of the patient/parent trio identified a *de novo* heterozygous c.1201G>A, p.Gly401Ser *DNM1L* variant (NM_012062.5). The *de novo* heterozygous *DNM1L* c.1201G>A, p.Gly401Ser missense variant was classified as 'likely pathogenic' using the Association of Clinical Genomic Science (ACGS) and The American College of Medical Genetics and Genomics (ACMG) guidelines (Richards *et al*, 2015) (https://www.acgs.uk.com/media/11631/uk-practice-guidelines-for-variant-classification-v4-01-2020.pdf) to apply the following criteria: PS2_moderate, PS3_moderate, PM2_moderate, PM4_supporting and PP4_supporting.

Analysis of muscle DNA from P2 showed no evidence of mtDNA copy number abnormalities or mtDNA rearrangements, while sequencing of the entire mtDNA genome revealed no variants of pathological significance. On account of the apparent respiratory chain defect involving complex I, a targeted Ampliseq capture was used to facilitate analysis of the coding regions of the known nuclear-encoded complex I subunits and assembly factors (50 genes). Annotation and filtering of patient variants was performed as previously described (Alston *et al*, 2016) and identified a single, novel heterozygous variant c.152G>A, p.Arg51Gln in *NDUFS5* (NM_004552.3), which encodes a structural subunit of complex I. The c.152G>A, p.Arg51Gln variant was initially categorised as a 'variant of uncertain significance' according to the ACGS/ACMG criteria PS2_moderate, PM2_moderate, PS3_supporting, PP3_supporting and PP4_supporting. Patient cDNA studies showed no other variants in the fibroblast-derived *NDUFS5* cDNA transcript. Analysis of parental samples by Sanger sequencing supported a *de novo* occurrence. Concurrent unbiased trio WES analysis of P2 and her parents was performed which revealed an additional *de novo* heterozygous variant, c.1088G>A, p.Gly363Asp in *DNM1L*. This variant was classified as 'likely pathogenic' using the ACGS/ACMG criteria PS2_moderate, PS3_supporting, PM2_moderate, PP3_supporting and PP4_supporting. In light of the c.1088G>A p.Gly363Asp *DNM1L* variant identified in P2, the c.152G>A p.Arg51Gln *NDUFS5* variant was subsequently reinvestigated - 4 heterozygote individuals are now recorded on gnomAD (two of which are adults) which is contraindicative of a dominantly-acting pathogenic variant meaning that the PM2 criterion is no longer applicable. Moreover, in light of an alternative

diagnosis *(DNM1L*-related disease), the guidelines support application of the BP5 criterion which reclassifies the c.152G>A p.Arg51Gln *NDUFS5* variant as 'likely benign'.

Initial investigations for P3 including mtDNA genome analysis and mtDNA copy number analysis were normal. P3 was subsequently enrolled onto the Genomics England 100,000 genome sequencing project, with targeted data analysis focusing on the gene panels for hereditary ataxia (v1.51) and paediatric motor neuronopathies (v1.0). Comparative genomic hybridization assay revealed a chromosome 19p13.3 microduplication that was not present in either parent, but its significance was uncertain. This analysis identified a single heterozygous c.687_689dup, p.Leu230dup *DNM1L* variant and analysis of parental samples supported a *de novo* occurrence. The 687_689dup, p.Leu230dup variant was classified as 'likely pathogenic' using the ACGS/ACMG criteria PS2_moderate, PS3_moderate, PM2_moderate, PM4_supporting and PP4_supporting.

Initial diagnostic investigations for P4 excluded the presence of common pathogenic *POLG* variants or a pathogenic mtDNA variant. Subsequently, trio WES analysis of P4 and his parents identified a single heterozygous c.2128A>G, p.Arg710Gly *DNM1L* variant that had arisen *de novo* in the proband. The c.2128A>G, p.Arg710Gly variant was classified as 'likely pathogenic' using the ACGS/ACMG criteria PS2_moderate, PS3_moderate, PM2_moderate, PP3_supporting and PP4_supporting.

Finally, DNA from P5 was subject to singleton WES analysis which revealed the same single heterozygous c.1201G>A, p.Gly401Ser *DNM1L* variant that was present in P1.

All *DNM1L* variants have not been previously reported pathogenic and were absent from gnomAD database (https://gnomad.broadinstitute.org/). The *DNM1L* variants were confirmed by Sanger sequencing and analysis of parental samples was undertaken either as part of the trio WES pipeline, or by targeted Sanger sequencing which supported the *de novo* occurrence of a *DNM1L* variant in each clinically-affected child.

In silico structural modelling of *DRP1* variants

Three of the five patients (P1, P2 and P5) exhibited single nucleotide variations, c.1201G>A, p.Gly401Ser (G401S) or c.1088G>A, p.Gly363Asp (G363D), in the DRP1 stalk domain (**Fig 1B**) which has been shown to play a key role in dimerization and self-assembly essential for fission (Francy *et al*, 2017; Fröhlich *et al*, 2013; Kalia *et al*, 2018). Analysis of the cryoEM structure of DRP1 in co-complex with one of its recruiting proteins, MID49 (PDB:5WP9), suggests that both residues are located at the dimer interface (**Fig 2A)**. Indeed, a quadruple mutant G401-404 AAAA has been shown to promote disruption of tetramers (or

any higher order oligomers) and the formation of stable dimers under certain conditions for DRP1 and other dynamin related proteins (Fröhlich *et al*, 2013; Gao *et al*, 2010; Faelber *et al*, 2011; Gao *et al*, 2011; Ford *et al*, 2011). The shared variant in P1 and P5 involves residue G401 which serves as a C-terminal capping residue for α-helix 1 in the stalk domain. Glycine is the most common C-terminal capping residue as it can adopt a wide range of phi psi angles due to its small, single hydrogen containing R-group, allowing for termination of a helix (Aurora *et al*, 1994; Richardson & Richardson, 1988; Bang *et al*, 2006; Beck *et al*, 2008). In the 5WP9 structure, G401 adopts a phi angle of 78.3º and psi angle of -160º (Fröhlich *et al*, 2013), a generally unfavourable conformation for residues other than glycine, which likely allows it to form a sharp helix-turn-helix, a prevalent structural motif in DRP1. Conversely, serine has a limited number of preferred phi psi angles (Beck *et al*, 2008) and a G401S substitution would likely result in an energetically unfavourable eclipsed conformation of the R group and adjacent amino or carbonyl groups. This would almost certainly introduce significant steric clashes, slightly destabilize the helix, and may impact self-assembly.

Regarding P2, G363 is an N-terminal alpha-helix capping residue and is in close proximity (4.2 Å) to the G401 residue of a neighbouring monomer (**Fig 2B**). Like the G401S substitution described above, G363 has relatively uncommon phi psi angles of -107.6º and -82.6º, respectively. The substitution of G363 to a larger charged aspartic acid, which does not typically populate those phi psi angles (Beck *et al*, 2008), would likely induce significant steric clashes with several nearby residues, including G401 and P402 (inter-molecular clashes) and E349 (intra-molecular clash). This could in turn disturb local secondary structure due to alpha-helix destabilization, as well as DRP1 dimerization. However, given the residue is adjacent to a flexible loop, one could predict that this region may be able to accommodate minor structural changes with no effects on dimer stability.

In P3, there is an insertion of an extra leucine at position 231 (L230dup) within the GTPase domain (**Fig 1B**), in a short alpha-helix that is flanked by two disordered loops, the canonical G4 (N-terminal of Leu230) and G5 (C-terminal of L230) motifs. The G4 and G5 motifs (**Fig 2C**) are critical for nucleotide binding (Wenger *et al*, 2013) and it is possible that the L230 duplication transmits a conformational change to these proximal loops and critical nucleotide binding residues such as K216, D218 and N246, impacting their GTP binding ability. In addition, dimerization *via* the GTPase domain is essential for GTP hydrolysis, and L230/L231 is spatially located near the alpha-helix containing the critical dimerization residue D190 (Wenger *et al*, 2013; Kishida & Sugio, 2013). Introduction of the extra leucine

at position 231 has the potential to introduce conformational changes in nearby regions, such as the adjacent G4 and G5 motifs or to the D190 containing helix, which may ultimately impair GTPase domain dimerization. Furthermore, the areas surrounding the L230/L231 residues of wild type DRP1 engage in an extensive interface with MID49 (**Fig 2D**) (Kalia *et al*, 2018). This interface is also mediated in part by the N-terminal loop of this region, specifically residue D221 of the G4 loop, which may be impaired by the L230 duplication. Altogether, these predictions suggest multiple mechanisms by which the L230dup event may lead to impaired DRP1 activity.

In P4, the residue R710 is located within the bundle signalling element (BSE) domain (**Fig 1B**), a highly conserved position among the dynamin superfamily (Sever *et al*, 1999; Muhlberg *et al*, 1997; Fröhlich *et al*, 2013; Zhu *et al*, 2004; Gao *et al*, 2011; Faelber *et al*, 2011; Ford *et al*, 2011; Gao *et al*, 2010). R710 forms a salt bridge with E702 in the C-terminal loop $L2^{BS}$ which is part of a highly conserved hinge motif between the GTPase and stalk domains (Fröhlich *et al*, 2013b). Substitution of this charged arginine to a small non-polar glycine would induce a loss of this salt bridge, likely leading to decreased protein stability and altered conformation of the hinge (**Fig 2E**). In dynamin and the human myxovirus resistance protein 1 (MxA), both of which belong to the dynamin superfamily of large GTPases, the hinge region is thought to facilitate conformational changes that lead to assembly stimulated GTP hydrolysis (Fröhlich *et al*, 2013; Gao *et al*, 2011; Sever *et al*, 1999). Crystallographic structure data of DRP1 revealed monomers with two different conformations, differing in their positioning of the GTPase domain and BSE in relation to the stalk, suggesting that similar large scale conformational changes around this hinge region are possible, and may relay assembly information to the GTPase domain in a similar manner (Fröhlich *et al*, 2013). Therefore, the disruption in stability would likely have a negative impact on DRP1 assembly-stimulated hydrolysis.

Mitochondrial and peroxisomal network analysis of *DNM1L* patient fibroblasts

Impaired mitochondrial fission due to defective DRP1 results in altered mitochondrial networks that are characterised by elongated and highly interconnected filamentous mitochondria. To assess the impact of the *DNM1L* variants identified in P1 (p.Gly401Ser), P2 (p.Gly363Asp), P3 (p.Leu230dup) and P4 (p.Arg710Gly) on mitochondrial morphology, live mitochondrial networks in available patient-derived fibroblasts were visualised using high-resolution confocal imaging after incubation with tetramethylrhodamine (TMRM), a cell

permeant dye that is actively sequestered into mitochondria on the basis of the membrane potential.

Analysis of mitochondrial networks using the ImageJ tool Mitochondrial Network Analysis (MiNA) revealed marked hyperfusion of mitochondria in P1, P2 and P4 compared to age-matched controls (**Fig 3A-B**). In addition, the mitochondrial network length was analysed using immunofluorescence labelling of fixed patient and age-matched control fibroblasts using TOM20 antibodies. The Columbus (Perkin Elmer) software system was used to quantify the hyperfusion of patient mitochondrial networks relative to controls. A minimum of 5,500 mitochondria were analysed for each case. Largely consistent with live cell imaging, significant hyperfusion of mitochondrial networks were observed in all four studied patient fibroblasts using this approach (**Fig 3C**). Whereas live cell imaging did not reveal extensive mitochondrial hyperfusion in P3 fibroblasts, TOM20 immunostaining revealed elongated mitochondria in P3 (p.Leu230dup) cells. Notably, these cells were the least affected compared to those from other patients (**Fig 3C**).

To determine if mitochondrial network alterations were due to decreased DRP1 recruitment, we performed a co-localisation analysis using the Pearson's co-localisation coefficient between DRP1 and TOM20 which showed decreased DRP1 at the mitochondria in P1 (p.Gly401Ser), P2 (p.Gly363Asp) and P4 (p.Arg710Gly) fibroblasts. Of these, P4 (p.Arg710Gly) had the most severe recruitment defect with the lowest Pearson's R value and DRP1 appearing primarily cytosolic without punctate structures; which were still seen in other variants albeit to a lesser extent than the control fibroblasts **(Fig 3D**).

Although the degree of mitochondrial hyperfusion differed between patient fibroblasts, with P3 (p.Leu230dup) not displaying significant elongation by MiNA, this phenotype was consistent with previously reported *de novo* heterozygous *DNM1L* variants (c.95G>C, p.Gly32Ala; c.436G>A, p.Asp146Asn; c.1184C>A, p.Ala395Asp; c.1207C>T, p.Arg403Cys; c.1292G>A, p.Cys431Tyr) and a GTPase deficient recombinant mutant (p.Lys38Ala) (Whitley *et al*, 2018; Longo *et al*, 2020; Chang *et al*, 2010; Waterham *et al*, 2007; Zhu *et al*, 2004).

Given DRP1 has been implicated in both mitochondrial and peroxisomal fission (Waterham *et al*, 2007), we examined the effect of these variants on peroxisomal networks. Immunofluorescence labelling of control and *DNM1L* patient fibroblasts with antibodies against the peroxisomal membrane protein marker PMP70 was used to determine the peroxisomal morphology. The analysis using the Columbus software revealed that peroxisomes in P1 (p.Gly401Ser), P2 (p.Gly363Asp), P3 (p.Leu230dup) and P4

(p.Arg710Gly) appeared more fused with fewer overall numbers of peroxisomes and decreased size distribution, indicative of impaired fission (**Fig 4A**).

Co-localisation analysis between DRP1 and PMP70 showed decreased DRP1 at the peroxisomes in P1 (p.Gly401Ser) and P2 (p.Gly363Asp), but not P3 (p.Leu230dup) and P4 (p.Arg710Gly), suggesting that the elongated peroxisomes in P3 and P4 are not simply due to decreased DRP1 recruitment (**Fig 4B**). Previous reports argue that not all *DNM1L* variants impair peroxisomal morphology, with several other variants in the GTPase domain having no impact on peroxisomal morphology despite affecting mitochondrial network morphology. Specifically, the p.Glu2Ala, p.Ala192Glu, (Gerber *et al*, 2017) and p.Gly32Ala (Whitley *et al*, 2018) variants had normal peroxisomes in the setting of abnormal mitochondrial networks. Conversely, patient fibroblasts from a bi-allelic heterozygous patient carrying p.Ser36Gly; p.Glu116Lysfs*6 variants had both abnormal peroxisomal and mitochondrial fission (Nasca *et al*, 2016). Similar impairments were also observed in the p.Asp146Asn (Longo *et al*, 2020) and p.Gly223Val variants (Verrigni *et al*, 2019). (**Table S1**).

Mitochondrial DNA nucleoid analysis of *de novo DNM1L* variants

Defective mitochondrial fission has also been associated with the formation of enlarged bulb-like structures (‘mito-bulbs’) caused by nucleoid clustering (Ban-Ishihara *et al*, 2013). Previously, *DNM1L* siRNA knockdown in HeLa cells as well as *Dnm1l*$^{-/-}$ knockout mice studies have demonstrated severe mtDNA nucleoid aggregation within the hyperfused mitochondrial networks, leading to respiratory deficiency and heart dysfunction in the fission-deficient mice (Ban-Ishihara *et al*, 2013; Ishihara *et al*, 2015). Imaging of fibroblasts incubated with TMRM revealed the presence of enlarged mitochondria in all patients (**Fig S1A**), with P1 (p.Gly401Ser) and P2 (p.Gly363Asp) most widely affected. Subsequent co-staining of P1 and P2 fibroblasts with TMRM and PicoGreen (a fluorochrome which reveals nucleoids by illuminating mtDNA) demonstrated the co-localisation of these enlarged ‘mito-bulbs’ with large nucleoids (**Fig S1B**). Detailed analysis of mtDNA nucleoids stained with PicoGreen using Columbus software (PerkinElmer) revealed marked differences in the proportion of enlarged nucleoids (area > 1.5μm^2) in P1 (p.Gly401Ser) and P2 (p.Gly363Asp) compared to control (**Fig S1C**). There was no difference in nucleoid size ratio between P3 (p.Leu230dup) and control (**Fig S1C**). Although, upon visual examination P4 (p.Arg710Gly) nucleoids appeared enlarged compare to controls, we were not able to accurately quantify the individual puncta due to increased levels of lipofuscin present in these cells (**Fig S1D**).

Altogether, assessment of patient fibroblasts demonstrated that the *de novo* variants identified in P1 (p.Gly401Ser) and P2 (p.Gly363Asp) cause mitochondrial network hyperfusion, leading to mitochondrial enlargement and nucleoid clustering which is indicative of impaired nucleoid distribution and segregation.

The effect of *DNM1L* variants on DRP1 protein expression

To evaluate the molecular consequences of the c.1201G>A, p.Gly401Ser; c.1088G>A, p.Gly363Asp; c.687_689dupATT, p.Leu230dup and c.2128A>G, p.Arg710Gly DRP1 variants, primary patient fibroblasts (P1-P4) and age-matched controls (C1-C4) were analysed by SDS-PAGE and immunoblotting (**Fig S4**). Normal levels of DRP1 protein in the monomeric form were found in P1 (p.Gly401Ser), P2 (p.Gly363Asp) and P3 (p.Leu230dup), whilst P4 (p.Arg710Gly) showed decreased levels of DRP1 when compared to controls (**Fig S2**). These data suggest that the mutated p.Gly401Ser, p.Gly363Asp and p.Leu230dup DRP1 protein is expressed in P1, P2 and P3, respectively, and may act in a dominant negative fashion, overriding the effect of the wild type allele. DRP1 recruitment to the mitochondrial membrane is dependent on adaptor proteins such as MID49 and MID51. However, their role in disease remains largely unclear. It has recently been described that MID51 regulates the assembly and fission activity of DRP1 (Ma et al, 2019). Western blot analysis of *DNM1L* patient fibroblasts revealed that levels of MID51 are similar in both patient and control fibroblasts (**Fig S2**), suggesting that the *DNM1L* variants do not affect the stability of the MID51 adaptor protein.

Diagnostic histological and biochemical investigations

Diagnostic respiratory chain enzyme analysis of cytochrome *c* oxidase (COX) and succinate dehydrogenase in P1 (p.Gly401Ser) muscle revealed decreased complex IV activity (**Table 1**). A quadruple immunofluorescent (IHC) assay, which quantifies protein levels of COX1, NDUFB8, porin and laminin in individual myofibres (Rocha *et al*, 2015), detected complex I-immunodeficient muscle fibres in P2 (p.Gly363Asp) (**Fig S3).** In addition, diagnostic spectrophotometric biochemical measurements of mitochondrial respiratory chain complex activities in the available muscle from P2 (p.Gly363Asp), P3 (p.Leu230dup) and P4 (p.Arg710Gly) were determined (**Fig S4A**). P2 (p.Gly363Asp) muscle showed decreased activities of complex I and complex II, whilst the activities of complexes III and IV were normal (**Fig S4A).** Two separate muscle biopsies have been taken in P3 (p.Leu230dup) at the age of 13 and 16 years old, respectively. The spectrophotometric respiratory chain complex

activities were normal in the first muscle biopsy, however the latter one showed a complex I and complex IV deficiency, suggesting a progressive defect (**Fig S4A**). Mitochondrial respiratory chain activities in P4 (p.Arg710Gly) skeletal muscle were normal, except for increased complex III activity, which may be attributed to a compensatory response mechanism (**Fig S4A**).

Variants in *DNM1L* impair levels of OXPHOS proteins

Next, we determined whether the mitochondrial network anomalies present in *DNM1L* patient fibroblasts were associated with OXPHOS dysfunction. Western blotting and quantification of bands obtained by densitometry analysis of P1 (p.Gly401Ser) fibroblasts revealed that the steady-state levels of OXPHOS proteins were relatively normal, except for mild decreases in complex I subunit, NDUFB8 and the complex IV subunit COX2 (**Fig S5**), which was consistent with the observed decreased complex IV activity in muscle tissue (**Table 1**). P2 (p.Gly363Asp) mutant fibroblasts presented with a decrease in NDUFB8, UQCRC2 and COX2 protein levels (**Fig S5**). In addition, the marked decrease in NDUFB8 protein levels detected by Western blotting correlate with the impaired complex I activity in patient-derived muscle and fibroblasts (**Fig S4A-B**). NGS analysis of P2 also identified a *de novo* heterozygous c.152G>A, p.Arg51Gln variant in the *NDUFS5* gene encoding a core accessory subunit of complex I. The c.152G>A, p.Arg51Gln *NDUFS5* variant could partially contribute to the decreased levels of NDUFB8 protein and impaired complex I activity, however *in silico* pathogenicity assessment classified the variant as likely benign and not pathogenic. A multiple OXPHOS defect was present in P3 (p.Leu230dup) fibroblasts, showing decreased steady state levels of NDUFB8, UQCRC2 and COX2 (**Fig S5**), where only impaired complex I and complex IV activity, correlated with the respiratory chain measurements in muscle (2^{nd} biopsy) (**Fig S4A**). Furthermore, a decrease in complex I (NDUFB8) and complex IV (COX2) subunits was detected in P4 (p.Arg710Gly) fibroblasts when compared to controls (**Fig S5**). Similar to the increased complex III activity in P4 muscle tissue (**Fig S4A**), densitometry analysis of the complex III subunit in P4 fibroblasts showed mild increase in the steady state levels of UQCRC2 (**Fig S5**).

Interestingly, there are some differences between the OXPHOS abnormalities amongst the patient muscle samples and fibroblasts. Most notably, P4 (p.Arg710Gly) whom had increased complex III activity in skeletal muscle, but decreased complex I and IV in fibroblasts. We hypothesize that these differences likely stem from tissue-specific effects on respiration. Together these data suggest that different *DNM1L* variants have distinct impact

on OXPHOS function in fibroblasts, with minimal correlations to disease onset or severity, suggesting that the OXPHOS defects present in cells are a secondary consequence of the disrupted mitochondrial network balance as opposed to a driver of disease.

Patient DRP1 variants have altered GTPase activity

DRP1 performs its mechanoenzyme function of mitochondrial membrane constriction through the hydrolysis of GTP following its assembly on the mitochondrial outer membrane. To determine whether *DNM1L* variants altered GTPase activity *in vitro*, we first expressed human DRP1 in recombinant form recapitulating the disease-causing variants identified in P1 and P5 c.1201G>A, p.Gly401Ser (G401S), P2 c.1088G>A, p.Gly363Asp (G363D), P3 c.687_689dupATT, p.Leu230dup (L230dup) and P4 c.2128A>G, p.Arg710Gly (R710G). Bacterial expression of all variants were similar to wild type (WT), except for L230dup which did not produce any full-length protein under multiple conditions and was unable to be purified for further studies. Wild type human DRP1 and the remaining variants were purified to homogeneity and found to be well folded by circular dichroism (**Fig S6**), but differences in the mean residue ellipticity suggested differences in structure that might affect GTP hydrolysis. To test this, GTP hydrolysis was measured in solution with increasing amounts of GTP substrate to determine the apparent Michaelis constant ($K_{0.5}$), the turnover number (k_{cat}), and catalytic efficiency ($k_{cat}/K_{0.5}$) (**Fig 5A-D**). The activity of WT enzyme was similar to previous measurements (Cahill *et al*, 2015; Chang *et al*, 2010; Francy *et al*, 2017; Fröhlich *et al*, 2013; Bustillo-Zabalbeitia *et al*, 2014; Koirala *et al*, 2013) with a $K_{0.5}^{GTP}$ of 201 ± 51 μM, a k_{cat} of 0.24 min^{-1}, and $k_{cat}/K_{0.5}$ of 1.2 x 10-3 $\mu M^{-1} \bullet min^{-1}$ (**Fig 5B-D** and **Table 2**). These substrate kinetic experiments with DRP1 variants G363D, G401S and R710G demonstrated modestly altered GTPase activity with R710G decreasing, and G363D and G401S increasing, the turnover number (**Fig 5A**). Curiously, each variant decreased the $K_{0.5}$ for GTP suggesting they modestly increased the catalytic efficiency for G363D and G401S, but not R710G. Overall these data suggest that impaired hydrolysis is not a major factor in pathogenesis of patients harbouring these variants. Although not tested, we predict the duplication of L230 would be deleterious to GTPase activity given the potential for direct disruption to the adjacent G4 and G5 loop motifs involved in nucleotide binding, or potential shifting of the interaction domains of DRP1 (i.e., GTPase domain, GED and/or stalk).

Patient DRP1 variants have impaired self-assembly

DRP1 assembles in the cytoplasm and around the circumference of the mitochondrion to effect membrane scission. To evaluate the pathological variants ability to self-assemble, we used size-exclusion chromatography with multi-angle laser light scattering (SEC-MALS, **Fig 6A**). This method is advantageous over traditional size exclusion chromatography as it allows for the direct determination of molecular weight instead of relying on comparisons to molecular weight standards with different molecular conformations that can influence their elution time (Some *et al*, 2019). Wild type DRP1 was found to primarily elute in two peaks corresponding to dimeric (elution time ~9 minutes) and tetrameric (elution time ~8 minutes) populations (**Fig 6A**), consistent with previous findings (Chang *et al*, 2010; Fröhlich *et al*, 2013; Macdonald *et al*, 2016; Francy *et al*, 2017). The range of molecular weight species observed on the chromatogram were interpreted to be due to a dynamic exchange between the oligomeric states during elution.

Each of the patient DRP1 variants was found to impair higher-order assembly to differing degrees, as determined by a decrease in the amount of higher molecular weight species eluting at earlier time points. Both G363D and G401S appear to be primarily dimeric, confirming previous studies on G363D (Chang *et al*, 2010; Clinton *et al*, 2016; Tanaka *et al*, 2006). Further, each of the variants altered the elution profile in that there was only one primary peak *versus* the more complex elution profile of wild type DRP1, suggesting that these substitutions alter the exchange rate between oligomeric species. Alterations to the elution profile and thus rates of exchange between species, have been observed before with G363D, as well as other stalk domain variants including the lethal A395D substitution and G350D (Chang *et al*, 2010). Notably, R710G had an earlier peak elution time than G363D and G401S, 8.79 minutes *versus* 9.07 and 8.99 minutes, respectively. This suggests that R710G likely retains some ability to assemble into higher-order oligomeric species, observed as a leftward shift in the peak elution time due to fast-exchange between dimeric and tetrameric species, contrary to G363D and G401S. In addition, treatment of total cell lysates derived from control and *DNM1L* patient fibroblasts with a chemical cross-linker BMH (bismaleimidohexane) resulted in increased formation of higher order oligomeric DRP1 complexes in P4 (**Fig S7**). Therefore, these data further support our SEC-MALS results, suggesting that the R710G variant retains more ability to assemble with wild type DRP1 than other variants. Together, these results provide strong evidence that these disease-causing variants alter DRP1 ability to assemble, which is critical for mediating mitochondrial fission.

Patient DRP1 variants are well-folded but have differing stability

Protein stability was evaluated using a fluorophore-based (SYPRO Orange) thermal shift assay and revealed the presence of two unfolding events in wild type DRP1 (**Fig 6B**). Repeating the assay in the presence of either 500 μM GDP or 500 μM GMP-PNP showed increased stability of the first unfolding event upon nucleotide binding, but not the second. Therefore, we interpreted the first and second transitions as corresponding to the unfolding of the GTPase and stalk domains, respectively. Given the variable domain of DRP1 is intrinsically disordered (Strack & Cribbs, 2012; Rosdah *et al*, 2020; Wenger *et al*, 2013; Fröhlich *et al*, 2013; Mahajan *et al*, 2021), it is not surprising that a third unfolding event corresponding to this domain was not observed given no significant loss of secondary structure would be expected in this region upon unfolding. Both G363D and G401S were found to have only one distinct unfolding event corresponding to GTPase domain unfolding, consistent with the SEC-MALS data showing no higher order organization. For wild type, addition of GDP had little effect on the stalk domain transitions as expected (**Fig 6C-D**). By contrast, addition of GDP significantly increased the T_m of the GTPase domain even more than GMP-PNP (**Fig 6C-D**), consistent with the known higher affinity of GDP over non-hydrolyzable GTP analogues for the GTPase domain (Fröhlich *et al*, 2013). This overall pattern was the same for all constructs indicating each variant is able to bind nucleotide, although DRP1 R710G showed a significantly lower GTPase domain melting temperature than WT, G363D and G401S, even in the presence of nucleotide, indicating that this variant destabilized the protein but not its ability to respond to nucleotide.

Discussion

Here, we report the discovery of five patients with previously unreported variants in *DNM1L*, including only the second GED domain variant (p.Arg710Gly) to be identified to date. The p.Gly363Asp variant has previously been studied given its high degree of conservation across species, although this is the first report of a patient harbouring this pathogenic variant to our knowledge (Kwapiszewska *et al*, 2019; Tanaka *et al*, 2006; Kobayashi *et al*, 2007; Otera *et al*, 2010; Chang *et al*, 2010). The variants described here were predicted to be 'likely pathogenic' according to ACGS guidelines, taking into account various criteria including variant allele frequency, functional studies, phenotypic fit and *in silico* predictions. *In silico* structural analysis of each variant concurred and predicted likely impairment of DRP1 oligomerisation (L230dup, G363D and G401S), GTP hydrolysis (L230dup and R710G) and protein stability (R710G) (Fröhlich *et al*, 2013; Kalia *et al*, 2018). Analysis of mitochondrial network morphology in fixed patient-derived cell lines revealed

impaired mitochondrial fission leading to hyperfused mitochondrial networks (**Fig 3C**) and in some cases enlarged mtDNA nucleoids (**Fig S1**), confirming dysfunctional DRP1 as the primary pathogenic factor in these patients. Furthermore, *DNM1L* variants present in P1 (p.Gly401Ser), P2 (p.Gly363Asp), P3 (p.Leu230dup) and P4 (p.Arg710Gly) also impaired normal peroxisomal fission (**Fig 4A**), which is not surprising given DRP1's prominent role in this process (Tanaka *et al*, 2006; Kobayashi *et al*, 2007; Otera *et al*, 2010; Yamano *et al*, 2014; Koch & Brocard, 2012; Koch *et al*, 2005; Li & Gould, 2003; Gandre-Babbe & Van Der Bliek, 2008). P1 (p.Gly401Ser), P2 (p.Gly363Asp) and P4 (p.Arg710Gly) *DNM1L* variants caused decreased DRP1 recruitment to the mitochondria (**Fig 3D**), but only P1 and P2 had decreased DRP1-peroxisome co-localisation (**Fig 4B**), suggesting that impaired DRP1 p.Arg710Gly peroxisomal fission occurs through a different mechanism. These data indicate that p.Arg710Gly mediated impairments are not simply due to a lack of DRP1 at the peroxisomal membrane, but may be due to impaired enzyme function with preservation of DRP1-peroxisome recruiter interactions, which are lost with the p.Gly363Asp and p.Gly401Ser variants.

To evaluate the effects of these mutations on DRP1, we performed a series of experiments designed to elucidate the specific mechanisms underpinning impaired function. The GTP hydrolysis activity is essential for DRP1 function. Interestingly, we found that G363D and G401S had increased GTP hydrolytic activity compared to WT DRP1, whereas R710G had decreased activity (**Fig 5A**). Previous studies examining the G363D variant have reported mixed hydrolysis results including no effect on hydrolytic activity (Clinton *et al*, 2016), or impaired hydrolysis (Chang *et al*, 2010; Tanaka *et al*, 2006). Given these discrepancies, it can't be ruled out that differences in GTP hydrolysis may be due to variations in recombinant protein constructs or preparation methods (e.g. DRP1 isoforms, N-*versus* C-terminal tags, calmodulin *versus* histidine purification tags) (Clinton *et al*, 2020). One might anticipate that increased GTP hydrolysis would result in increased fission intracellularly. However, it is possible that these results are representative of futile GTP cycling in which G363D and G401S retain hydrolytic capabilities but are unable to assemble into the higher order oligomeric species.

Both G363D and G401S appear to be in mutational hotspots (**Fig 1B**) with multiple variants in nearby regions reported including: G350R, G362S, G362D, A395D, A395G, R403C, L406S and E410K (Chang *et al*, 2010; Whitley *et al*, 2018; Sheffer *et al*, 2016; Verrigni *et al*, 2019; Vanstone *et al*, 2016; Fahrner *et al*, 2016; Ryan *et al*, 2018; Zaha *et al*, 2016; Vandeleur *et al*, 2019). These variants reside spatially close to each other within the

stalk domain of the protein, a region important for mediating protein oligomerisation (Francy *et al*, 2017; Fröhlich *et al*, 2013), which in turn is critical for stabilization of DRP1-MFF complexes post recruitment to the mitochondria (Clinton *et al*, 2016) as well as assembly with MID49 (Kalia *et al*, 2018). This suggests the variants may have impaired fission secondary to diminished higher-order assembly and/or poor recruitment to the mitochondria secondary to impaired DRP1-recruiter interactions. Consistent with this, both p.Gly363Asp and p.Gly401Ser have decreased DRP1 at the mitochondria as determined by DRP1-TOM20 co-localisation analysis (**Fig 3D**). Therefore, the decrease in mitochondrial fission despite increased GTP hydrolysis for both G363D and G401S likely stems from a lack of DRP1 recruitment and productive fission activity at the mitochondria.

In addition, our SEC-MALS data suggest that both G363D and G401S are unable to attain higher-order species as they eluted in a primarily dimeric population (**Fig 6A**), consistent with previous reports on G363D (Chang *et al*, 2010; Clinton *et al*, 2016; Kwapiszewska *et al*, 2019). The glycine at position 401 is one of four highly conserved amino acids (GPRP, 401-404) located at the assembly interface where it is involved in mediating oligomerisation of proteins within the Dynamin superfamily including dynamin, DRP1 and MxA (Gao *et al*, 2010; Faelber *et al*, 2011; Ford *et al*, 2011). Like dynamin, these four residues required mutation to AAAA to prevent oligomerisation and inherent disorder of the loop region to achieve crystallization of DRP1 (Fröhlich *et al*, 2013). Therefore, it is likely that both substitutions directly impair higher order assembly and may also disrupt local secondary structure given these variants did not exhibit a clear unfolding of the stalk domain by thermal shift analysis.

From a clinical mitochondrial disease perspective, it is interesting that both P1 (c.1201G>A, p.Gly401Ser) and P2 (c.1088G>A, p.Gly363Asp) exhibited cardiac complications, including end stage dilated cardiomyopathy with previous signs of hypertrophic cardiomyopathy in P1. Of the previously reported variants, c.1228G>A, p.Glu410Lys is the only pathogenic human *DNM1L* variant that has been reported to result in severe cardiac involvement, which ultimately resulted in death of the patient at 8 months of age (Vandeleur *et al*, 2019). Cardiac involvement in patients with *DNM1L*-related mitochondrial disease has previously been postulated, since a C452F substitution in mouse DRP1 (position p.Cys446Phe in human DRP1 NP_036192.2) was shown to cause dilated cardiomyopathy (Cahill *et al*, 2015). Concordantly, a three-month old patient who initially presented with infantile parkinsonism like symptoms was identified to possess the same C446F substitution and died at 2.5 years of age due to sudden cardiac arrest (Díez *et al*,

2017). However, no post-mortem evaluation was performed to determine the cause of cardiac arrest. It would therefore seem appropriate that patients with confirmed pathogenic *DNM1L* variants follow a cardiac surveillance programme, as is in place for other forms of mitochondrial disease, with a view to appropriate pre-emptive treatment.

In general, pathogenic variants involving the stalk domain of DRP1 also appear to be more severe than those affecting the GTPase domain which primarily present as optic abnormalities with or without concurrent neurological and developmental findings (Gerber *et al*, 2017; Whitley *et al*, 2018; Wei & Qian, 2021; Longo *et al*, 2020; Hogarth *et al*, 2018). We note a similar trend in our cohort with P1, P5 (c.1201G>A, p.Gly401Ser) and P2 (c.1088G>A, p.Gly363Asp) experiencing an earlier onset of more severe symptoms, faster disease progression and early death, whereas P3 (c.687_689dupATT, p.Leu230dup) and P4 (c.2128A>G, p.Arg710Gly) had a later onset and lived to an older age. Of note, P3 (p.Leu230dup) and P4 (p.Arg710Gly) also exhibited less severe peroxisomal defects compared to P1 (p.Gly401Ser) and P2 (p.Gly363Asp). It may be that concurrent mitochondrial and peroxisomal defects lead to more severe phenotypes and disease progression. Consistent with this, several other non-lethal DRP1 variants, located primarily in the GTPase domain, resulted in cells with normal peroxisome morphology despite having impaired mitochondrial networks (Gerber *et al*, 2017; Whitley *et al*, 2018; Chao *et al*, 2016) (**Table S1**).

In true peroxisomal biogenesis disorders (PBDs), lipid metabolism, among other peroxisome-related metabolic pathways, is impaired. Clinically, *DNM1L* and PBD patients have phenotypic overlap including developmental delays, seizures, hypotonia, facial dysmorphism and vision impairment. Unlike PBD patients though, *DNM1L* patients do not typically develop renal or hepatic dysfunction, skeletal abnormalities, or cataracts (Waterham & Ebberink, 2012). Given these similarities, and the peroxisome fission abnormalities in many *DNM1L* patients, one might hypothesize that *DNM1L* patients would display similar biochemical profiles, with elevated very long-chain and branched-chain fatty acids (De Biase *et al*, 2019). Unfortunately, there remains a dearth of *DNM1L* patient reports that analyse both peroxisomal morphology and perform the necessary analyses to fully evaluate peroxisomal function. Based on data currently available, there is not a clear correlation between laboratory findings, peroxisome morphology, and disease severity with some variants displaying normal peroxisome morphology with normal laboratory tests p.Gly362Ser (Sheffer *et al*, 2016), normal peroxisomes with elevated plasma VLCFA and normal pristanic acid (p.Gly32Ala) (Whitley *et al*, 2018), abnormal peroxisomes with normal laboratory tests

(p.Ser36Gly, p.Glu116Lysfs*6; p.Gly362Ser; p.Ile512Thr, p.Gly362Asp; p.Gly350Arg and p.Tyr691Cys) (Nasca *et al*, 2016; Verrigni *et al*, 2019; Chao *et al*, 2016), and abnormal peroxisomes with abnormal lab tests (p.Ala395Asp) (Waterham *et al*, 2007). Several studies noted abnormal peroxisomal morphology but did not perform lipid profiling (Longo *et al*, 2020; Chao *et al*, 2016; Zaha *et al*, 2016) and it is unclear whether these patients may have had abnormal results (**Table S1**). Although traditional peroxisome functional tests may not be fruitful diagnostically, future studies using lipidomic approaches may capture more nuanced metabolic changes that occur, identifying potential biomarkers for *DNM1L*-associated disease with peroxisome involvement. Ultimately, *DNM1L* disorders appear to derive primarily from mitochondrial defects and the degree of peroxisome-driven pathology remains unclear, but likely secondary.

Unfortunately, we were unable to obtain full-length recombinant DRP1 L230dup (P3) for *in vitro* studies. Given this residue's relative proximity to the nucleotide binding site, a duplication event is likely to disrupt GTP binding. This would have direct impacts on GTP hydrolysis and resulting fission activity. DRP1 L230 is also near the DRP1-MID49 interface and the duplication may selectively inhibit recruiter interactions. Currently, only the structure of DRP1 in complex with MID49 has been solved (Kalia *et al*, 2018), so it is possible that other recruiting proteins bind at alternate locations enabling residual DRP1 activity to be performed. Alternatively, and contrasting a dominant negative mechanism, this allele is catalytically dead and residual DRP1 activity is maintained by the wild type allele. In support of this, patient fibroblasts demonstrated a milder hyperfusion of mitochondrial reticula compared to the other variants and they lived to 20 years of age suggesting slower disease progression.

Intramolecular interaction between a monomer's GTPase Effector Domain (GED), the N-terminal GTPase domain and stalk domain, as well as interactions between adjacent GEDs, are essential for regulation of DRP1 GTP hydrolysis (Pitts *et al*, 2004; Chang & Blackstone, 2007; Zhu *et al*, 2004). This is a common feature in all dynamin proteins (Zhang & Hinshaw, 2001; Muhlberg *et al*, 1997; Smirnova *et al*, 1999; Sever *et al*, 1999; Schumacher & Staeheli, 1998; Di Paolo *et al*, 1999; Shin *et al*, 1999) where removal of the GED in dynamin or DRP1 does not prevent nucleotide binding or higher-order assembly but decreases GTPase activity (Muhlberg *et al*, 1997; Zhu *et al*, 2004). Similarly, R710G can still bind GTP, evidenced by its ability to hydrolyze GTP and stabilization of the GTPase domain upon nucleotide binding, but has decreased GTPase activity. Mutation of R725 in dynamin (R710 in human DRP1 (NP_036192.2) and both located in the hinge 1 region) prevents

stimulation of GTPase activity by the GED domain, suggesting it is a key residue involved in sensing and transmitting assembly information to the GTPase domain (Sever *et al*, 1999). The hinge 1 region has also been shown to be important for MxA function which shares structural properties with the family of dynamin-like GTPases. However, disruption of MxA R640 or E632 (equivalent to R710 and E676 in human DRP1 (NP_036192.2)) impairs higher-order oligomerisation and decreased the off-rate of GTP, thus causing increased GTP hydrolysis which is opposite of what is observed in dynamin (Gao *et al*, 2011; Sever *et al*, 1999). Nearby dynamin residue K694 (equivalent human DRP1 residue: K679) is also located in the GED, but mutation results in impaired assembly, suggesting it lays at the interface between adjacent GEDs where it stabilizes their interaction during assembly (Sever *et al*, 1999). A previously reported *de novo* p.Tyr691Cys DRP1 variant in the fifth alpha-helix of the stalk portion of the GED was proposed to disrupt GED-GTPase interactions (Batzir *et al*, 2019), but it seems more likely that this substitution would negatively impact GED-GED assembly given its location at this interface. Interestingly, the c.2072A>G, p.Tyr691Cys *DNM1L* patient and our c.2128A>G, p.Arg710Gly (P4) had similar, less severe phenotypes compared to stalk domain variants and presented with epilepsy, optic atrophy, impaired mobility and prominent cyclical vomiting.

Therefore, we predict that R710G is pathogenic due to a disruption in the sensing mechanism that facilitates assembly-driven increases in GTP hydrolysis. Further, this variant had the greatest loss of recruitment to the mitochondria in patient fibroblasts, suggesting this process, or region of the protein, may be important for proper DRP1-mitochondrial recruiter recognition. It is unclear if the substitution results in direct disruption of GED-GTPase domain interaction, or if it is a downstream mechanism. Supporting a direct disruption, R710G results in a lower Tm for the GTPase domain, albeit with retained nucleotide binding capabilities, reflective of decreased protein stability, possibly due to loss of the intramolecular GED-GTPase domain interactions. It is therefore not surprising that this patient had lower protein levels of DRP1 and this may be reflective of increased protein degradation secondary to the decreased stability; whereas the other patients did not, suggesting haploinsufficiency is not a major driver of pathology in those cases, which has been noted for other variants as well (Whitley et al, 2018). R710G is perhaps somewhat assembly deficient compared to wild type, but more assembled than G363D or G401S and is found in a dynamic equilibrium between a dimeric and tetrameric state.

There are nine known DRP1 isoforms that arise from differential splicing in the GTPase or variable domains, with isoforms differing based on their inclusion, or lack of, a 13

amino acid insert in the GTPase domain (A insert) and a partial or full 37 amino acid insert in the variable domain (B insert) (Rosdah *et al*, 2020). These isoforms have varying GTPase rates in the presence of cardiolipin, a primary component of the mitochondrial outer membrane, or in response to the DRP1 recruiter MFF (Macdonald *et al*, 2016). Currently, none of the reported variants are found within the A or B insert, suggesting all DRP1 isoforms in patients would be affected. This raises the question of why neuronal tissue is predominantly affected in this patient population. It may be that certain isoforms are more tolerant of substitutions, experiencing fewer or less severe impacts on protein oligomerisation or GTP hydrolysis. Genetic mosaicism may also play a role in patients with milder, or perhaps even subclinical, phenotypes. It is also unclear why fetal development is grossly normal given the preponderance of heterozygous dominance among *DNM1L* variants. A role for DRP1 in development is still emerging, but evidence supports the importance of DRP1 as global knockout is embryonic lethal in mouse models (Ishihara *et al*, 2009; Wakabayashi *et al*, 2009).

Here, we have described with mechanistic precision how pathogenic variants disrupt DRP1 biophysical activity and lead to mitochondrial hyperfusion. We document that divergent mechanisms including combinations of aberrant stability, organellar recruitment, assembly, and GTPase activity contribute to pathogenesis caused by mutations in different domains of DRP1. In summary, a thorough understanding of how DRP1 function is impaired in human disease will provide insight into the diverse phenotypes and variable disease severity associated with pathogenic *DNM1L* variants. A systematic characterisation of patient presentation and progression will assist in the timely identification of other patients with rare *DNM1L* variants, while understanding the specific molecular mechanisms underlying DRP1 function will promote the development of targeted therapeutics with a goal of restoring mitochondrial fission to non-pathological levels. Crucially, our work details the first example of a patient with a *DNM1L* variant in the hinge region which will be crucial to answering an outstanding question: how assembly information is transmitted to the GTPase domain to stimulate GTP hydrolysis in the dynamin superfamily.

Materials and Methods

Ethical Statement

Written informed consent for diagnostic molecular genetic analysis and research-based studies was obtained from all patients in accordance with the Declaration of Helsinki protocols and ethical approvals of local institutional review boards.

Diagnostic studies of skeletal muscle biopsies

Available skeletal muscle biopsies were subjected to routine diagnostic investigations, including diagnostic TEM studies of muscle from P1. Diagnostic *in vitro* spectrophotometric measurements of respiratory chain complex activities were undertaken in P2, P3 and P4 muscle according to standard procedures (Kirby *et al*, 2007). Complex I and IV immunodeficient muscle fibres in P2 were determined by a quadruple fluorescent IHC assay of OXPHOS function, which evaluates protein levels of mitochondrial subunits of complex I (NDUFB8) and complex IV (COX1). In addition to the immunofluorescence labelling of muscle sections using antibodies against the above described OXPHOS complexes, the mitochondrial mass was quantified using an antibody against the outer mitochondrial membrane protein – porin (VDAC) and the myofibre boundaries were labelled with anti-laminin, a membrane glycoprotein as previously described (Rocha *et al*, 2015).

Molecular genetics studies

All patients underwent routine mtDNA diagnostic testing that excluded variants in the mitochondrial genome. Next generation sequencing strategies followed by filtering and candidate variant analysis were undertaken to elucidate the molecular bases of studies mitochondrial disease patients. GnomAD (https://gnomad.broadinstitute.org/) database was used for minor allele frequency (MAF) analysis (≤0.01 %). *In silico* pathogenicity tools were used to assess the pathogenicity of candidate variants and classified as 'likely pathogenic' using the Association of Clinical Genomic Science (ACGS) and The American College of Medical Genetics and Genomics (ACMG) guidelines (Richards *et al*, 2015) (https://www.acgs.uk.com/media/11631/uk-practice-guidelines-for-variant-classification-v4-01-2020.pdf).

Family trio whole exome sequencing (WES) analysis was performed on P1 using the Agilent Sure Select Human All Exon Kit v6 according to manufacturer's instructions, followed by sequencing on an Illumina NextSeq platform. For P2, targeted NGS sequencing using a custom 84.38 Kb Ampliseq panel (Life Technologies) was initially performed to capture relevant regions of 50 Complex I genes as previously described (Alston *et al*, 2016). Sequencing was performed using the Ion PGM 200 Sequencing Kit on an Ion Torrent PGM

Sequencer. Variant calling was undertaken using the proprietary IonTorrent Variant Caller plugin and sequence variants were annotated using wANNOVAR for prioritisation and classification. Further to targeted NGS, trio WES analysis was performed using Agilent SureSelectXT All Exon v.5 according to manufacturer's instructions, followed by sequencing on an Illumina HiSeq2500 platform and in-house pipelines were used for variant calls as previously described (Taylor *et al*, 2014; Rocha *et al*, 2015). For P3, whole genome sequencing was performed by Genomics England via the 100,000 genomes project. WES and variant filtering and prioritization was performed in P4 as previously described (Thompson *et al*, 2016; Taylor *et al*, 2014). WES analysis was also performed on P5 as described in P1 using the Agilent Sure Select Human All Exon Kit v6 and sequencing on an Illumina NextSeq platform.

In silico analysis and structural modelling

The structures of DRP1 (PDB: 4BEJ), DRP1 in complex with GDP.AIF4 (3W6P), DRP1 in complex with GMP-PCP (3W6O) and co-assembled DRP1-MID49 (PDB: 5WP9) were used to assess the structural implications of the patient mutations using PyMOL by Schrödinger (https://pymol.org/2/). *In silico* mutagenesis was performed using Modeler software with standard parameters (https://salilab.org/modeller/).

Cell lines

Primary patient fibroblasts and age-matched controls were grown in high-glucose Dulbecco's Modified Eagle Medium (Gibco) supplemented with 10% (v/v) fetal bovine serum (FBS), 1% non-essential amino acids, 1.0 mM sodium pyruvate, 50 µg/ml uridine, 50 U/ml penicillin and 50 µg/ml streptomycin at 37 °C in an atmosphere of 5.0 % CO_2. All primary control and patient fibroblasts used in this study were under P0+12 passages.

Mitochondrial network analysis using the Mitochondrial Analysis (MiNa)

Asynchronized control and patient fibroblasts were cultured overnight on 35 mm Ibidi m-dishes (Ibidi, 88156) before incubation in 0.15% PicoGreen (Invitrogen P7581) for 30 mins, then washed and incubated in 5.0 nM TMRM (Invitrogen T668) for 30 minutes. Z-stack images were taken on a VisiTech iSIM with a 100x objective before processing using Fiji to generate maximum projection images. These images were analysed using the Mitochondrial Analysis (MiNa) tool on Fiji and for each image the mean mitochondrial network length calculated by multiplying the mean branch length by the mean number of

branches per network. Statistically significant differences were calculated via non-parametric one-way ANOVA and Dunn's multiple comparisons using GraphPad Prism.

Analysis of mtDNA nucleoids, mitochondrial network and peroxisomal morphology using the Columbus system

Cells were synchronised overnight by starvation using DMEM media with 0.1% FBS (Mitra *et al*, 2009). G0-arrested cells were plated out on to 96-well plates and cultured in DMEM containing 10% FBS for 24 hours before incubation with 0.15% PicoGreen (Invitrogen P7581) for 30 mins at 37 °C. Following three washes in Flurobrite DMEM (Fisher Scientific A1896701) Z-stack images were taken on a Zeiss CellDiscoverer7 microscope with 50x water objective (NA 1.2). Maximum projection images were analysed using the Columbus (PerkinElmer) software system and for each image field the proportion of enlarged nucleoids classed as over 1.5μm^2 were calculated in the total nucleoid pool. Statistically significant differences were calculated via non-parametric one-way ANOVA using GraphPad Prism.

For immunofluorescence analysis cells were synchronised as described above and fixed with 4% paraformaldehyde in 1x phosphate-buffered saline (PBS) for 15 min at 37 °C. Following three washes in PBS, cells were incubated for 10 minutes with 50 mM NH_4Cl to quench the paraformaldehyde, washed 3 times in PBS and permeabilized with 0.1% Triton X-100 in PBS for 10 min at room temperature (RT). Subsequently, cells were washed three times with PBS, blocked with 5% FBS in PBS for 10 minutes at RT, and incubated with primary antibodies in diluted blocking buffer overnight at 4 °C. Primary antibodies [anti-DRP1 BD Biosciences #611113 (1:500 dilution), anti-TOM20 Santa Cruz sc-17764 (1:500 dilution), anti-TOM20 Abcam ab186735 (1:2000 dilution) and anti-PMP70 Abcam ab3421 (1:3000 dilution)] were washed off with PBS (3x 5 minutes) and appropriate secondary antibodies conjugated to Alexa Fluor 488 or 647 (1:1000 dilution Molecular Probes, Invitrogen) and Hoechst 33342 (ThermoFisher) stain (1:5000 dilution) were applied for 1hr at RT. Following 3x 5 minutes washes with PBS, cells were analysed using a Zeiss CellDiscoverer7 microscope. Z-stack images were taken with a 50x water objective (NA 1.2) before maximum-intensity projections were analysed using Columbus (Perkin Elmer) for mitochondrial and peroxisomal network length and mtDNA nucleoids size. Statistically significant differences in mitochondrial network length were calculated via non-parametric one-way ANOVA using GraphPad Prism.

Immunofluorescence DRP1 co-localisation studies

For DRP1 co-localisation studies synchronised cells were labelled with antibodies against DRP1, TOM20 and PMP70 as described above. Images were prepared for co-localisation analysis in Fiji (ImageJ) using two separate ImageJ macros: one to split channels into separate folders and one to generate stacks of Z-projections for each channel as well as a merged max-intensity projection image of all three channels (Schindelin *et al*, 2012) (https://github.com/Hill-Lab/DNM1L-Variants-Scripts). For the cells immunostained with anti-PMP70, the same ImageJ macros were used but included a separate rotation (1-2°) and crop step to correct for slight skewing of the stitched images. Cells were outlined to create regions of interest (ROIs) using the software CellProfiler (McQuin *et al*, 2018). Single channel maximum-intensity projection images were corrected for illumination variations and primary objects were classified as nuclei using adaptive Otsu thresholding on the DAPI channel. Secondary objects were classified as cells using the DRP1 channel with nuclei as the input objects. For cells co-stained with anti-TOM20, cells were identified using the Watershed-Image feature of CellProfiler with the Global Minimum Cross-Entropy thresholding method. Cell outlines for cells co-stained with PMP70 were created using the same method except no illumination variation correction was performed and cells were identified using the adaptive Otsu thresholding method.

Cell outlines were exported as a .png image file and used as the regions of interest (ROIs) for co-localisation analysis in ImageJ. Cell outlines were visually inspected and cells that were not adequately outlined were corrected manually in ImageJ. The ImageJ coloc2 plugin was then used to calculate the Pearson's Correlation between endogenous DRP1 and either endogenous TOM20 or endogenous PMP70 using the selected ROI regions from the maximum intensity projection images. RStudio (1.4.1106) (RStudio Team, 2021) was used to tidy and compile this data using tidyverse 1.3.0 (Wickham, 2017), plot as box plots using ggplot2 (3.3.3) (Wickham, 2016), and perform one-way ANOVA with post-hoc Tukey's Honest Significant Difference test (https://github.com/Hill-Lab/DNM1L-Variants-Scripts).

Protein expression and purification

Recombinant DRP1 isoform 1 was expressed using a pET29b+ vector as a $DRP1^{1-736}$–His_6 fusion protein in BL21(DE3) *E. coli* as previously described (Bordt *et al*, 2017; Cahill *et al*, 2015). Transformed cells were grown at 37 °C in Luria broth containing kanamycin (30 g/ml) to an OD_{600} of ~ 1.0 with 0.5 mM isopropyl 1-thio-b-D-

galactopyranoside (IPTG). After 16-18 h, cells were harvested by centrifugation and resuspended in Buffer A (20 mM HEPES pH 7.4, 500 mM NaCl, 40 mM imidazole, 0.02% sodium azide) containing protease inhibitors (Roche Applied Science). Cells were lysed with an EmulsiFlex C3 homogenizer (Avestin) at 15,000 p.s.i. and protein lysate was clarified through centrifugation at 15,000 rpm for 45 minutes at 4 ºC using a JA–20 rotor in a Beckman J2–21 centrifuge. Clarified lysate was applied to a nickel affinity column (Sepharose high performance beads, GE Healthcare) equilibrated in Buffer A using an FPLC. The column was washed with 10 column volumes each of Buffers B (20 mM HEPES pH 7.4, 500 mM NaCl, 40 mM imidazole, 10 mM KCl, 1.0 mM ATP, 0.02% sodium azide) and C (20 mM HEPES pH 7.4, 500 mM NaCl, 40 mM imidazole, 0.5% (w/v) CHAPS, 0.02% sodium azide). Protein was eluted with Buffer D (20 mM HEPES pH 7.4, 500 mM NaCl, 500 mM imidazole, 0.02% sodium azide) and peak fractions were pooled, concentrated to ~ 1.0 – 2.0 mL using Vivaspin 20 centrifugal concentrators (GE Healthcare) with a molecular weight cut-off of 50 kDa and dialyzed overnight at 4 ºC in GTPase reaction Buffer (20 mM HEPES pH 7.4, 150 mM KCl, 2.0 mM $MgCl_2$, 1.0 mM DTT, 0.5 mM EDTA, 0.02% sodium azide). Protein concentration was determined by measuring absorbance at 280 nm in the presence of 6.0 M guanidine HCl with a theoretical extinction coefficient of 35,870.96. Protein was then flash frozen in liquid nitrogen in single use 100 – 200 µL aliquots and stored at -80 ºC. All studied DRP1 variants were obtained through Quickchange mutagenesis (Stratagene) with a pET29b+–$DRP1^{1–736}$ (isoform 1) construct (primers available upon request). DRP1 variants were induced with 0.25 mM IPTG and otherwise expressed and purified akin to DRP1–WT.

GTPase activity measurements

DRP1 GTPase activity was measured using a continuous, regenerative coupled GTPase assay which reports on GTP hydrolysis that is directly proportional to the depletion of NADH (Ingerman & Nunnari, 2005). Depletion of NADH was measured at Abs_{340} for 45 minutes at 25 ºC using a Molecular Devices (Sunnyvale, CA) FlexStation 3 Multi–Detection Reader with Integrated Fluid Transfer. Reactions (150 µL) of 1.0 µM DRP1 (WT or variant) and 150 mM NaCl were performed in a flat–bottom 96–well plate (Corning Costar) in GTPase reaction buffer (25 mM HEPES pH 7.4, 10 mM $MgCl_2$, 1.0 mM phosphoenolpyruvate (PEP), 7.5 mM KCl, 0.8 mM NADH, 20 units/mL pyruvate kinase/lactate dehydrogenase) at the following GTP concentrations: 0, 10, 30, 70, 100, 300, 500, 700, 1000, 1300, 1700 and 2000 µM. Reactions were started by addition of 10 µL of 15x concentrated GTP stocks to each well. Data were imported into RStudio (1.4.1106)

(RStudio Team, 2021) using readxl (1.3.1) (Wickham & Brian, 2019) and tidied using tidyverse (1.3.0) (Wickham, 2017). Depletion of NADH at Abs_{340} were converted to GTPase activity rates using equation 1 and kinetic parameters were determined through global fitting the data to a Michaelis-Menten model (equation 2). Activity from each DRP1 variant was collected from three independent preparations and are reported as means ± standard deviation. Statistical significance of $K_{0.5}$ was determined by a one–way ANOVA followed by Tukey's Honest Significant Difference test. Plots were generated in RStudio using ggplot2 (3.3.3) (Wickham, 2016), gridExtra (2.3) (Baptiste, 2017), and RColorBrewer (1.1-2) (Neuwirth, 2014) (https://github.com/Hill-Lab/DNM1L-Variants-Scripts).

Eq. (1): GTPase activity (min^{-1}) = $\frac{\Delta Abs340}{min} / (\frac{6220}{Mcm} * p / \frac{1e6\mu M}{M}) / [DRP1]$

where ΔAbs340 = change in Abs at 340 nm for the steady state linear depletion, Vol = volume of reaction, which is 150 µL here, 6220/Mcm = extinction coefficient of NADH, [DRP1] = concentration of DRP1 used in assay, which was 1.0 µM unless otherwise noted and p = path length of well, which was determined to be 0.4649 cm in our assay set–up.

Eq. (2): $V_0 = \frac{V_{max} * [GTP]}{[GTP] + K_{0.5}}$,

where V_0 = initial velocity of reaction, V_{max} = maximal velocity of reaction, [GTP] = concentration of GTP (i.e., substrate) and $K_{0.5}$ = value of [GTP] at V_0 = 0.5*V_{max} and is a generalized Michaelis-Menten constant.

Eq. (3): $k_{cat} = \frac{Vmax}{[DRP1]}$

Where V_{max} = maximal velocity of reaction, [DRP1] = concentration of DRP1 used in assay, which was 1.0 µM.

Size Exclusion Chromatography with Multiangle Laser Light Scattering and Differential Refractive Index

Wild-type and variant $DRP1^{1-736}$-His6 fusion proteins were purified as described above. Aliquots (400 uL total volume) were thawed on ice and dialyzed overnight at 4°C into column running buffer (20 mM HEPES, pH 7.4, 150 mM KCl, 2.0 mM $MgCl_2$, 0.5 mM EDTA, 1.0 mM DTT, 0.02% sodium azide filtered through a 0.02 micron filter using vacuum filtration). Protein concentrations were determined as stated above following dialysis.

Samples were injected (100 uL of 3.0 mg/mL) and chromatographed at 1.0 mL/min at 25°C on a BioSep HPLC size exclusion column (BioSep-SEC-S 4000, 300 x 7.8 mm) equilibrated with column running buffer with a guard column (08543-TSKgel Guard SWXL, 6.0 mm ID x 4.0 cm, 7.0 µM) in place. The eluate was detected using a DAWN-EOS multiangle laser light scattering instrument and the Optilab refractive index detector (Wyatt Technologies, Santa Barbara, CA). Data analysis was performed using the ASTRA software package (Wyatt Technologies). Data were imported into RStudio (1.4.1106) (RStudio Team, 2021) and tidied as described above. Traces were then normalized and centre-scaled to allow for easier comparison using caret (6.0-86) (Kuhn, 2020). Chromatograms were then generated using ggplot2 (3.3.3) (Wickham, 2016) and RColorBrewer (1.1-2) (Neuwirth, 2014) and plotted with molar mass (right axis) and normalized and scaled dRI (left axis) as a function of time (x axis) (https://github.com/Hill-Lab/DNM1L-Variants-Scripts). Chromatograms are representative of two independent protein preparations for wild-type and each variant.

Thermal Shift Assay

Reactions (30 µL) consisting of 5.0 µM DRP1 (WT or variant) and 5x SYPRO orange (excitation 470 nm/emission 570 nm) in DRP1 GTPase reaction buffer (20 mM HEPES, pH 7.4, 150 mM KCl, 2.0 mM $MgCl_2$, 1.0 mM DTT, 0.5 mM EDTA, 0.02% sodium azide) ± 500 µM GDP or 500 µM GMP-PNP were set-up in a 0.1 mL x 96-well white non-skirted PCR plate (PR1MA PR-PCR1196-W). Both GDP and GMP-PNP stock solutions were prepared in DRP1 GTPase reaction Buffer (20 mM HEPES pH 7.4, 150 mM KCl, 2.0 mM $MgCl_2$, 1.0 mM DTT, 0.5 mM EDTA, 0.02% sodium azide) to the target concentration. PCR plates were heat treated at 95°C for 30 minutes to prevent SYPRO orange from interacting with polyethylene in plate giving erroneous fluorescence readings at 57°C. Protocol adapted from Huynh and Partch (Huynh & Partch, 2015). SYPRO orange fluorescence was measured in one-minute intervals with a temperature ramp of 1°C per minute using a Stratagene Thermoler Mx3005P. Data were imported into RStudio (1.4.1106) (RStudio Team, 2021) and tidied as described above. Melting temperatures (T_m) were determined by the temperature corresponding to the maximum value of the 1st derivative of the fluorescence signal. Statistical significance of T_m value alterations were determined by a one–way ANOVA followed by Tukey's Honest Significant Difference test. Plots were generated using ggplot2 (3.3.3) (Wickham, 2016) and RColorBrewer (1.1-2) (Neuwirth, 2014) with dFluorescence/dTime (y axis) as a function of time (x axis). Two biological replicates, each

with three technical replicates, were used for analysis and plot generation (https://github.com/Hill-Lab/DNM1L-Variants-Scripts).

Circular Dichroism

Far UV circular dichroism was performed on a Jasco J-1500 CD Spectrometer with 0.05 mg/mL DRP1 (WT and variant) at 20 °C using a 10 mm pathlength and 5 accumulation average. A continuous scanning mode at 100 nm/min with 3.0 nm bandwidth, 0.1 nm data interval from 190-300 nm was used. All samples were brought to an equivalent concentration in DRP1 GTPase reaction buffer (20 mM HEPES, pH 7.4, 150 mM KCl, 2.0 mM $MgCl_2$, 1.0 mM DTT, 0.5 mM EDTA, 0.02% sodium azide) and then diluted to their final concentration in double distilled 0.45 µm filtered H_2O to ensure equivalent concentrations of buffer components. Reference scans performed on each sample's empty cuvette, as well as a buffer only sample, were subtracted from the final signal to remove background ellipticity due to residual buffer components. Molar ellipticity was converted to mean residue ellipticity (equation 4) and data were scaled to a baseline of 0 at 260 nm using Microsoft Excel. Data were imported into RStudio (1.4.1106) (RStudio Team, 2021)and tidied as described above. Plots were generated using ggplot2 (3.3.3) (Wickham, 2016) and RColorBrewer (1.1-2) (Neuwirth, 2014) with CD signal in terms of mean residue ellipticity on the vertical axis and wavelength on the horizontal axis (https://github.com/Hill-Lab/DNM1L-Variants-Scripts). Protein concentrations were determined again after data collection using the absorbance and theoretical extinction coefficients at 205 nm and 214 nm to ensure equivalent amounts of protein were used.

Eq. (4): $\Omega = \frac{\theta * MRW}{10 * c * d}$

Where Ω = mean residue ellipticity, MRW = mean residue weight calculated as the protein Molecular Weight/(N-1) where N = total number of residues, c = concentration (mg/mL), and d = path length (cm).

Data Availability Statement

All R scripts used for data analysis and visualization are available upon request and/or for download at https://github.com/Hill-Lab/DNM1L-Variants-Scripts.

Acknowledgements

RM and RWT are supported by the Wellcome Centre for Mitochondrial Research (203105/Z/16/Z), Mitochondrial Disease Patient Cohort (UK) (G0800674), the Medical Research Council (MRC) International Centre for Genomic Medicine in Neuromuscular Disease (MR/S005021/1), the UK NIHR Biomedical Research Centre for Ageing and Age-related disease award to the Newcastle upon Tyne Foundation Hospitals NHS Trust and the UK NHS Highly Specialised Service for Rare Mitochondrial Disorders of Adults and Children. MO and RWT receive funding from the Pathology Society. RM, MO and RWT receive funding from the Lily Foundation. OMR is supported by the Wellcome Centre for Mitochondrial Research (203105/Z/16/Z). CLA is supported by a National Institute for Health Research (NIHR) Post-Doctoral Fellowship (PDF-2018-11-ST2-021). This project was also supported by the following National Institutes of Health grants: TL1TR001437 and T32GM080202 (to KAN), R01GM067180 (to RBH), and R01HL128240 (to MEW). The views expressed in this publication are those of the author(s) and not necessarily those of the National Health Service (NHS), the National Institute for Health Research (NIHR) or the Department of Health and Social Care. The content is solely the responsibility of the author(s) and does not necessarily represent the official views of the NIH.

We would like to thank Dr. Julien Prudent from the MRC Mitochondrial Biology Unit at University of Cambridge for constructive discussions about the project. We also thank Laura Bone for technical support and the Newcastle University Bioimaging Unit for assistance with the microscopy. We thank the Exeter Genomics Laboratory and the Gastroenterology team at Sheffield Children's Hospital for their support.

Authors Contributions

Kelsey A. Nolden – conceptualization, data curation, formal analysis, investigation, methodology, software and writing—original draft, review and editing.
John M. Egner – conceptualization, data curation, formal analysis, investigation, methodology and writing—original draft.
Jack J. Collier – data curation, formal analysis, investigation, methodology, software and writing—original draft.
Oliver M. Russell - formal analysis, software and investigation, writing – review and editing.
Charlotte L. Alston – formal analysis and investigation.
Megan C. Harwig – formal analysis, software and investigation.

Michael E. Widlansky – investigation

Souphatta Sasorith – software and formal analysis.

Inês A. Barbosa – formal analysis and investigation.

Andrew G. L. Douglas – investigation.

Julia Baptista – formal analysis and investigation.

Mark Walker – investigation.

Deirdre E. Donnelly – investigation.

Andrew A. Morris – investigation.

Hui Jeen Tan – formal analysis and investigation.

Manju A. Kurian - investigation.

Kathleen Gorman - formal analysis and investigation.

Santosh Mordekar - investigation.

Charu Deshpande - investigation.

Rajib Samanta – investigation.

Robert McFarland - investigation.

R. Blake Hill – investigation, funding acquisition, supervision, writing - review and editing

Robert W. Taylor – investigation, funding acquisition, data curation, supervision, writing - review and editing.

Monika Oláhová - conceptualization, investigation, data curation, formal analysis, methodology, supervision, funding acquisition, and writing—original draft, review, and editing.

Conflict of Interest

The authors have declared that no conflict of interest exists. RBH and KAN have a financial interest in Cytegen, a company developing therapies to improve mitochondrial function. However, neither the research described herein was supported by Cytegen, nor was is in collaboration with the company.

Alston CL, Howard C, Oláhová M, Hardy SA, He L, Murray PG, O'Sullivan S, Doherty G, Shield JPH, Hargreaves IP, *et al* (2016) Short report: A recurrent mitochondrial p.Trp22Arg NDUFB3 variant causes a distinctive facial appearance, short stature and a mild biochemical and clinical phenotype. *J Med Genet* 53: 634

Aouacheria A, Baghdiguian S, Lamb HM, Huska JD, Pineda FJ & Hardwick JM (2017) Connecting mitochondrial dynamics and life-or-death events via Bcl-2 family proteins. *Neurochem Int* 109: 141

Ashrafian H, Docherty L, Leo V, Towlson C, Neilan M, Steeples V, Lygate CA, Hough T, Townsend S, Williams D, *et al* (2010) A mutation in the mitochondrial fission gene Dnm1l leads to cardiomyopathy. *PLoS Genet* 6: 1–18

Aurora R, Srinivasan R & Rose GD (1994) Rules for α-helix termination by glycine. *Science (80-)* 264: 1126–1130

Ban-Ishihara R, Ishihara T, Sasaki N, Mihara K & Ishihara N (2013) Dynamics of nucleoid structure regulated by mitochondrial fission contributes to cristae reformation and release of cytochrome c. *Proc Natl Acad Sci U S A* 110: 11863

Bang D, Gribenko A V, Tereshko V, Kossiakoff AA, Kent SB & Makhatadze GI (2006) Dissecting the energetics of protein α-helix C-cap termination through chemical protein synthesis. *Nat Chem Biol 2006 23* 2: 139–143

Baptiste A (2017) gridExtra: Miscellaneous Functions for "Grid" Graphics. R package version 2.3.

Basu K, Lajoie D, Aumentado-Armstrong T, Chen J, Koning RI, Bossy B, Bostina M, Sik A, Bossy-Wetzel E & Rouiller I (2017) Molecular mechanism of {DRP1} assembly studied in vitro by cryo-electron microscopy. *PLoS One* 12: e0179397

Batzir NA, Bhagwat PK, Eble TN, Liu P, Eng CM, Elsea SH, Robak LA, Scaglia F, Goldman AM, Dhar SU, *et al* (2019) De novo missense variant in the GTPase effector domain (GED) of DNM1L leads to static encephalopathy and seizures. *Mol Case Stud* 5: a003673

Beck DAC, Alonso DO V., Inoyama D & Daggett V (2008) The intrinsic conformational propensities of the 20 naturally occurring amino acids and reflection of these propensities in proteins. *Proc Natl Acad Sci* 105: 12259–12264

De Biase I, Tortorelli S, Kratz L, J. Steinberg S, Cusmano-Ozog K & Braverman N (2019) Laboratory diagnosis of disorders of peroxisomal biogenesis and function: a technical standard of the American College of Medical Genetics and Genomics (ACMG). *Genet Med 2019 224* 22: 686–697

Bustillo-Zabalbeitia I, Montessuit S, Raemy E, Basañez G, Terrones O & Martinou J-C (2014) Specific Interaction with Cardiolipin Triggers Functional Activation of Dynamin-Related Protein 1. *PLoS One* 9: 102738

Cahill TJ, Leo V, Kelly M, Stockenhuber A, Kennedy NW, Bao L, Cereghetti G, Harper AR, Czibik G, Lao C, *et al* (2015) Resistance of Dynamin-related Protein 1 Oligomers to Disassembly Impairs Mitophagy, Resulting in Myocardial Inflammation and Heart Failure. *J Biol Chem* 290: 25907–25919

Cervantes-Silva MP, Cox SL & Curtis AM (2021) Alterations in mitochondrial morphology as a key driver of immunity and host defence. *EMBO Rep* 22

Chang C-R, Manlandro CM, Arnoult D, Stadler J, Posey AE, Hill RB & Blackstone C (2010) A lethal de novo mutation in the middle domain of the dynamin-related {GTPase} Drp1 impairs higher order assembly and mitochondrial division. *J Biol Chem* 285: 32494–32503

Chang CR & Blackstone C (2007) Cyclic AMP-dependent Protein Kinase Phosphorylation of Drp1 Regulates Its GTPase Activity and Mitochondrial Morphology. *J Biol Chem* 282: 21583–21587

Chao YH, Robak LA, Xia F, Koenig MK, Adesina A, Bacino CA, Scaglia F, Bellen HJ & Wangler MF (2016) Missense variants in the middle domain of DNM1L in cases of infantile encephalopathy alter peroxisomes and mitochondria when assayed in Drosophila. *Hum Mol Genet* 25: 1846–1856

Clinton RW, Bauer BL & Mears JA (2020) Chapter 4 Affinity Purification and Functional Characterization of Dynamin-Related Protein 1. In *Methods in molecular biology* pp 41–53. Clifton, N.J.

Clinton RW, Francy CA, Ramachandran R, Qi X & Mears JA (2016) Dynamin-related Protein 1 Oligomerization in Solution Impairs Functional Interactions with Membrane-anchored Mitochondrial Fission Factor. *J Biol Chem* 291: 478–492

Collier JJ & Taylor RW (2021) Machine learning algorithms reveal the secrets of mitochondrial dynamics. *EMBO Mol Med* 13: e14316–e14316

Díez H, Cortès-Saladelafont E, Ormazábal A, Marmiese AF, Armstrong J, Matalonga L, Bravo M, Briones P, Emperador S, Montoya J, *et al* (2017) Severe infantile parkinsonism because of a de novo mutation on DLP1 mitochondrial-peroxisomal protein. *Mov Disord* 32: 1108–1110

Dorn GW (2019) Evolving concepts of mitochondrial dynamics. *Annu Rev Physiol* 81: 1–17

Dorn GW, Vega RB & Kelly DP (2015) Mitochondrial biogenesis and dynamics in the developing and diseased heart. *Genes Dev* 29: 1981–1991 doi:10.1101/gad.269894.115 [PREPRINT]

Faelber K, Posor Y, Gao S, Held M, Roske Y, Schulze D, Haucke V, Noé F & Daumke O (2011) Crystal structure of nucleotide-free dynamin. *Nature* 477: 556–562

Fahrner JA, Liu R, Perry MS, Klein J & Chan DC (2016) A novel de novo dominant negative mutation in DNM1L impairs mitochondrial fission and presents as childhood epileptic encephalopathy. *Am J Med Genet Part A* 170: 2002–2011

Ford MGJ, Jenni S & Nunnari J (2011) The crystal structure of dynamin. *Nature* 477: 561–566

Francy CA, Clinton RW, Fröhlich C, Murphy C & Mears JA (2017) Cryo-EM Studies of Drp1 Reveal Cardiolipin Interactions that Activate the Helical Oligomer. *Sci Reports 2017 71* 7: 1–12

Friedman JR, Lackner LL, West M, DiBenedetto JR, Nunnari J & Voeltz GK (2011) ER Tubules Mark Sites of Mitochondrial Division. *Science* 334: 358

Fröhlich C, Grabiger S, Schwefel D, Faelber K, Rosenbaum E, Mears J, Rocks O & Daumke O (2013) Structural insights into oligomerization and mitochondrial remodelling of dynamin 1-like protein. *EMBO J* 32: 1280–1292

Gandre-Babbe S & Van Der Bliek AM (2008) The novel tail-anchored membrane protein Mff controls mitochondrial and peroxisomal fission in mammalian cells. *Mol Biol Cell* 19: 2402–2412

Gao S, von der Malsburg A, Paeschke S, Behlke J, Haller O, Kochs G & Daumke O (2010) Structural basis of oligomerization in the stalk region of dynamin-like MxA. *Nature* 465: 502–506

Gao S, von der Malsburg A, Dick A, Faelber K, Schröder GF, Haller O, Kochs G & Daumke O (2011) Structure of Myxovirus Resistance Protein A Reveals Intra- and Intermolecular Domain Interactions Required for the Antiviral Function. *Immunity* 35: 514–525

Gerber S, Charif M, Chevrollier A, Chaumette T, Angebault C, Kane MS, Paris A, Alban J, Quiles M, Delettre C, *et al* (2017) Mutations in DNM1L, as in OPA1, result indominant optic atrophy despite opposite effectson mitochondrial fusion and fission. *Brain* 140: 2586–2596

Harvey AJ (2019) Mitochondria in early development: linking the microenvironment,

metabolism and the epigenome. *Reproduction* 157: R159–R179
Hogarth KA, Costford SR, Yoon G, Sondheimer N & Maynes JT (2018) DNM1L Variant Alters Baseline Mitochondrial Function and Response to Stress in a Patient with Severe Neurological Dysfunction. *Biochem Genet* 56: 56–77
Horbay R & Bilyy R (2016) Mitochondrial dynamics during cell cycling. *Apoptosis* 21: 1327–1335
Huynh K & Partch CL (2015) Analysis of protein stability and ligand interactions by thermal shift assay. *Curr Protoc protein Sci* 79: 28.9.1-28.9.14
Ihenacho UK, Meacham KA, Harwig MC, Widlansky ME & Hill RB (2021) Mitochondrial Fission Protein 1: Emerging Roles in Organellar Form and Function in Health and Disease. *Front Endocrinol (Lausanne)* 12: 274
Ikeda Y, Shirakabe A, Maejima Y, Zhai P, Sciarretta S, Toli J, Nomura M, Mihara K, Egashira K, Ohishi M, *et al* (2015) Endogenous Drp1 mediates mitochondrial autophagy and protects the heart against energy stress. *Circ Res* 116: 264–278
Ingerman E & Nunnari J (2005) A continuous, regenerative coupled gtpase assay for dynamin-related proteins. In *Gtpases regulating membrane dynamics* pp 611–619. Elsevier
Ishihara N, Nomura M, Jofuku A, Kato H, Suzuki SO, Masuda K, Otera H, Nakanishi Y, Nonaka I, Goto YI, *et al* (2009) Mitochondrial fission factor Drp1 is essential for embryonic development and synapse formation in mice. *Nat Cell Biol* 11: 958–966
Ishihara T, Ban-Ishihara R, Maeda M, Matsunaga Y, Ichimura A, Kyogoku S, Aoki H, Katada S, Nakada K, Nomura M, *et al* (2015) Dynamics of mitochondrial DNA nucleoids regulated by mitochondrial fission is essential for maintenance of homogeneously active mitochondria during neonatal heart development. *Mol Cell Biol* 35: 211–223
James DI, Parone PA, Mattenberger Y & Martinou JC (2003) hFis1, a novel component of the mammalian mitochondrial fission machinery. *J Biol Chem* 278: 36373–36379
Kalia R, Wang RYR, Yusuf A, Thomas P V., Agard DA, Shaw JM & Frost A (2018) Structural basis of mitochondrial receptor binding and constriction by DRP1. *Nature* 558: 401–405
Kasahara A & Scorrano L (2014) Mitochondria: From cell death executioners to regulators of cell differentiation. *Trends Cell Biol* 24: 761–770 doi:10.1016/j.tcb.2014.08.005 [PREPRINT]
Kirby DM, Thorburn DR, Turnbull DM & Taylor RW (2007) Biochemical Assays of Respiratory Chain Complex Activity. *Methods Cell Biol* 80: 93–119
Kishida H & Sugio S (2013) Crystal structure of GTPase domain fused with minimal stalks from human dynamin-1-like protein (Dlp1) in complex with several nucleotide analogues. *Curr Top Pept Protein Res* 14: 67–77
Kobayashi S, Tanaka A & Fujiki Y (2007) Fis1, DLP1, and Pex11p coordinately regulate peroxisome morphogenesis. *Exp Cell Res* 313: 1675–1686
Koch A, Yoon Y, Bonekamp NA, McNiven MA & Schrader M (2005) A role for Fis1 in both mitochondrial and peroxisomal fission in mammalian cells. *Mol Biol Cell* 16: 5077–5086
Koch J & Brocard C (2012) PEX11 proteins attract Mff and human Fis1 to coordinate peroxisomal fission. *J Cell Sci* 125: 3813–3826
Koirala S, Guo Q, Kalia R, Bui HT, Eckert DM, Frost A & Shaw JM (2013) Interchangeable adaptors regulate mitochondrial dynamin assembly for membrane scission. *Proc Natl Acad Sci U S A* 110: E1342
Kraus F & Ryan MT (2017) The constriction and scission machineries involved in mitochondrial fission. *J Cell Sci* 130: 2953–2960

Kuhn M (2020) caret: Classification and Regression Training. R package version 6.0-86. https://CRAN.R-project.o [PREPRINT]

Kwapiszewska K, Kalwarczyk T, Michalska B, Szczepański K, Szymański J, Patalas-Krawczyk P, Andryszewski T, Iwan M, Duszyński J & Hołyst R (2019) Determination of oligomerization state of Drp1 protein in living cells at nanomolar concentrations. *Sci Reports 2019 91* 9: 1–9

Li X & Gould SJ (2003) The dynamin-like GTPase DLP1 is essential for peroxisome division and is recruited to peroxisomes in part by PEX11. *J Biol Chem* 278: 17012–17020

Liu T, Yu R, Jin SB, Han L, Lendahl U, Zhao J & Nistér M (2013) The mitochondrial elongation factors MIEF1 and MIEF2 exert partially distinct functions in mitochondrial dynamics. *Exp Cell Res* 319: 2893–2904

Liu X, Zhang Z, Li D, Lei M, Li Q, Liu X & Zhang P (2021) DNM1L-Related Mitochondrial Fission Defects Presenting as Encephalopathy: A Case Report and Literature Review. *Front Pediatr* 9: 626657

Longo F, Benedetti S, Zambon AA, Sora MGN, Di Resta C, De Ritis D, Quattrini A, Maltecca F, Ferrari M & Previtali SC (2020) Impaired turnover of hyperfused mitochondria in severe axonal neuropathy due to a novel DRP1 mutation. *Hum Mol Genet* 29: 177–188

Losón OC, Song Z, Chen H & Chan DC (2013) Fis1, Mff, {MiD49}, and {MiD51} mediate Drp1 recruitment in mitochondrial fission. *Mol Biol Cell* 24: 659–667

Ma J, Zhai Y, Chen M, Zhang K, Chen Q, Pang X & Sun F (2019) New interfaces on {MiD51} for Drp1 recruitment and regulation. *PLoS One* 14: e0211459

Macdonald PJ, Francy CA, Stepanyants N, Lehman L, Baglio A, Mears JA, Qi X & Ramachandran R (2016) Distinct Splice Variants of Dynamin-related Protein 1 Differentially Utilize Mitochondrial Fission Factor as an Effector of Cooperative {GTPase} Activity. *J Biol Chem* 291: 493–507

Mahajan M, Bharambe N, Shang Y, Lu B, Mandal A, Mohan PM, Wang R, Boatz JC, Galvez JMM, Shnyrova A V., *et al* (2021) NMR identification of a conserved Drp1 cardiolipin-binding motif essential for stress-induced mitochondrial fission. *Proc Natl Acad Sci* 118: e2023079118

McQuin C, Goodman A, Chernyshev V, Kamentsky L, Cimini BA, Karhohs KW, Doan M, Ding L, Rafelski SM, Thirstrup D, *et al* (2018) CellProfiler 3.0: Next-generation image processing for biology. *PLoS Biol* 16

Mears JA, Lackner LL, Fang S, Ingerman E, Nunnari J & Hinshaw JE (2011) Conformational changes in Dnm1 support a contractile mechanism for mitochondrial fission. *Nat Struct \& Mol Biol* 18: 20–26

Mishra P & Chan DC (2014) Mitochondrial dynamics and inheritance during cell division, development and disease. *Nat Rev Mol Cell Biol* 15: 634–646 doi:10.1038/nrm3877 [PREPRINT]

Mitra K, Wunder C, Roysam B, Lin G & Lippincott-Schwartz J (2009) A hyperfused mitochondrial state achieved at G1-S regulates cyclin E buildup and entry into S phase. *Proc Natl Acad Sci U S A* 106: 11960–11965

Muhlberg AB, Warnock DE & Schmid SL (1997) Domain structure and intramolecular regulation of dynamin GTPase. *EMBO J* 16: 6676–6683

Nagashima S, Tábara L-C, Tilokani L, Paupe V, Anand H, Pogson JH, Zunino R, McBride HM & Prudent J (2020) Golgi-derived PI (4) P-containing vesicles drive late steps of mitochondrial division. *Science* 367: 1366–1371

Nasca A, Legati A, Baruffini E, Nolli C, Moroni I, Ardissone A, Goffrini P & Ghezzi D (2016) Biallelic Mutations in DNM1L are Associated with a Slowly Progressive

Infantile Encephalopathy. *Hum Mutat* 37: 898–903

Neuwirth E (2014) RColorBrewer: ColorBrewer Palettes. R package version 1.1-2. https://CRAN.R-project.or [PREPRINT]

Otera H, Wang C, Cleland MM, Setoguchi K, Yokota S, Youle RJ & Mihara K (2010) Mff is an essential factor for mitochondrial recruitment of Drp1 during mitochondrial fission in mammalian cells. *J Cell Biol* 191: 1141–1158

Palmer CS, Osellame LD, Laine D, Koutsopoulos OS, Frazier AE & Ryan MT (2011) MiD49 and MiD51, new components of the mitochondrial fission machinery. *EMBO Rep* 12: 565–573

Pangou E & Sumara I (2021) The Multifaceted Regulation of Mitochondrial Dynamics During Mitosis. *Front Cell Dev Biol* 9

Di Paolo C, Hefti HP, Meli M, Landis H & Pavlovic J (1999) Intramolecular Backfolding of the Carboxyl-terminal End of MxA Protein Is a Prerequisite for Its Oligomerization. *J Biol Chem* 274: 32071–32078

Pitts KR, McNiven MA & Yoon Y (2004) Mitochondria-specific Function of the Dynamin Family Protein DLP1 Is Mediated by Its C-terminal Domains. *J Biol Chem* 279: 50286–50294

Qian W, Choi S, Gibson GA, Watkins SC, Bakkenist CJ & Van Houten B (2012) Mitochondrial hyperfusion induced by loss of the fission protein Drp1 causes {ATM}-dependent G2/M arrest and aneuploidy through {DNA} replication stress. *J Cell Sci* 125: 5745–5757

Richards S, Aziz N, Bale S, Bick D, Das S, Gastier-Foster J, Grody WW, Hegde M, Lyon E, Spector E, *et al* (2015) Standards and Guidelines for the Interpretation of Sequence Variants: A Joint Consensus Recommendation of the American College of Medical Genetics and Genomics and the Association for Molecular Pathology. *Genet Med* 17: 405

Richardson JS & Richardson DC (1988) Amino acid preferences for specific locations at the ends of α helices. *Science (80-)* 240: 1648–1652

Rocha MC, Grady JP, Grünewald A, Vincent A, Dobson PF, Taylor RW, Turnbull DM & Rygiel KA (2015) A novel immunofluorescent assay to investigate oxidative phosphorylation deficiency in mitochondrial myopathy: understanding mechanisms and improving diagnosis. *Sci Rep* 5

Rosdah AA, Smiles WJ, Oakhill JS, Scott JW, Langendorf CG, Delbridge LMD, Holien JK & Lim SY (2020) New perspectives on the role of Drp1 isoforms in regulating mitochondrial pathophysiology.

Roy M, Reddy PH, Iijima M & Sesaki H (2015) Mitochondrial division and fusion in metabolism. *Curr Opin Cell Biol* 33: 111–118 doi:10.1016/j.ceb.2015.02.001 [PREPRINT]

RStudio Team (2021) RStudio: Integrated Development Environment for R. RStudio, PBC, Boston, MA URL http://www.rstudio.co [PREPRINT]

Ryan CS, Fine AL, Cohen AL, Schiltz BM, Renaud DL, Wirrell EC, Patterson MC, Boczek NJ, Liu R, Babovic-Vuksanovic D, *et al* (2018) De Novo DNM1L Variant in a Teenager With Progressive Paroxysmal Dystonia and Lethal Super-refractory Myoclonic Status Epilepticus: *https://doi.org/101177/0883073818778203* 33: 651–658

Schindelin J, Arganda-Carreras I, Frise E, Kaynig V, Longair M, Pietzsch T, Preibisch S, Rueden C, Saalfeld S, Schmid B, *et al* (2012) Fiji - an Open Source platform for biological image analysis. *Nat Methods* 9: 676–682

Schumacher B & Staeheli P (1998) Domains Mediating Intramolecular Folding and Oligomerization of MxA GTPase. *J Biol Chem* 273: 28365–28370

Sever S, Muhlberg AB & Schmid SL (1999) Impairment of dynamin's GAP domain

stimulates receptor-mediated endocytosis. *Nat 1999 3986727* 398: 481–486

Sheffer R, Douiev L, Edvardson S, Shaag A, Tamimi K, Soiferman D, Meiner V & Saada A (2016) Postnatal microcephaly and pain insensitivity due to a de novo heterozygous {DNM1L} mutation causing impaired mitochondrial fission and function. *Am J Med Genet A* 170: 1603–1607

Shin HW, Takatsu H, Mukai H, Munekata E, Murakami K & Nakayama K (1999) Intermolecular and Interdomain Interactions of a Dynamin-related GTP-binding Protein, Dnm1p/Vps1p-like Protein. *J Biol Chem* 274: 2780–2785

Smirnova E, Griparic L, Shurland DL & Van der Bliek AM (2001) Dynamin-related protein Drp1 is required for mitochondrial division in mammalian cells. *Mol Biol Cell* 12: 2245–2256

Smirnova E, Shurland DL, Newman-Smith ED, Pishvaee B & Van Der Bliek AM (1999) A Model for Dynamin Self-assembly Based on Binding Between Three Different Protein Domains. *J Biol Chem* 274: 14942–14947

Some D, Amartely H, Tsadok A & Lebendiker M (2019) Characterization of Proteins by Size-Exclusion Chromatography Coupled to Multi-Angle Light Scattering (SEC-MALS). *J Vis Exp* 2019

Song M, Mihara K, Chen Y, Scorrano L & Dorn GW (2015) Mitochondrial fission and fusion factors reciprocally orchestrate mitophagic culling in mouse hearts and cultured fibroblasts. *Cell Metab* 21: 273–286

Stojanovski D, Koutsopoulos OS, Okamoto K & Ryan MT (2004) Levels of human Fis1 at the mitochondrial outer membrane regulate mitochondrial morphology. *J Cell Sci* 117: 1201–1210

Strack S & Cribbs JT (2012) Allosteric modulation of Drp1 mechanoenzyme assembly and mitochondrial fission by the variable domain. *J Biol Chem* 287: 10990–11001

Tanaka A, Kobayashi S & Fujiki Y (2006) Peroxisome division is impaired in a {CHO} cell mutant with an inactivating point-mutation in dynamin-like protein 1 gene. *Exp Cell Res* 312: 1671–1684

Taylor RW, Pyle A, Griffin H, Blakely EL, Duff J, He L, Smertenko T, Alston CL, Neeve VC, Best A, *et al* (2014) Use of whole exome sequencing to determine the genetic basis of multiple mitochondrial respiratory chain complex deficiency. *JAMA* 312: 68

Thompson K, Majd H, Dallabona C, Reinson K, King MS, Alston CL, He L, Lodi T, Jones SA, Fattal-Valevski A, *et al* (2016) Recurrent De Novo Dominant Mutations in SLC25A4 Cause Severe Early-Onset Mitochondrial Disease and Loss of Mitochondrial DNA Copy Number. *Am J Hum Genet* 99: 1405

Tilokani L, Nagashima S, Paupe V & Prudent J (2018) Mitochondrial dynamics: overview of molecular mechanisms. *Essays Biochem* 62: 341–360

Touvier T, De Palma C, Rigamonti E, Scagliola A, Incerti E, Mazelin L, Thomas J-LL, D'Antonio M, Politi L, Schaeffer L, *et al* (2015) Muscle-specific Drp1 overexpression impairs skeletal muscle growth via translational attenuation. *Cell Death Dis* 6: e1663–e1663

Vandeleur D, Chen C V., Huang EJ, Connolly AJ, Sanchez H & Moon-Grady AJ (2019) Novel and lethal case of cardiac involvement in DNM1L mitochondrial encephalopathy. *Am J Med Genet Part A* 179: 2486–2489

Vanstone JR, Smith AM, McBride S, Naas T, Holcik M, Antoun G, Harper ME, Michaud J, Sell E, Chakraborty P, *et al* (2016) DNM1L-related mitochondrial fission defect presenting as refractory epilepsy. *Eur J Hum Genet* 24: 1084–1088

Verrigni D, Di Nottia M, Ardissone A, Baruffini E, Nasca A, Legati A, Bellacchio E, Fagiolari G, Martinelli D, Fusco L, *et al* (2019) Clinical-genetic features and peculiar muscle histopathology in infantile DNM1L-related mitochondrial epileptic

encephalopathy. *Hum Mutat* 40: 601–618

Wai T & Langer T (2016) Mitochondrial Dynamics and Metabolic Regulation. *Trends Endocrinol Metab* 27: 105–117 doi:10.1016/j.tem.2015.12.001 [PREPRINT]

Wakabayashi J, Zhang Z, Wakabayashi N, Tamura Y, Fukaya M, Kensler TW, Iijima M & Sesaki H (2009) The dynamin-related GTPase Drp1 is required for embryonic and brain development in mice. *J Cell Biol* 186: 805–816

Waterham HR & Ebberink MS (2012) Genetics and molecular basis of human peroxisome biogenesis disorders. *Biochim Biophys Acta - Mol Basis Dis* 1822: 1430–1441

Waterham HR, Koster J, van Roermund CWT, Mooyer PAW, Wanders RJA & Leonard J V. (2007) A Lethal Defect of Mitochondrial and Peroxisomal Fission. *N Engl J Med* 356: 1736–1741

Wei Y & Qian M (2021) Case Report: A Novel de novo Mutation in DNM1L Presenting With Developmental Delay, Ataxia, and Peripheral Neuropathy. *Front Pediatr* 9: 604105

Wenger J, Klinglmayr E, Fröhlich C, Eibl C, Gimeno A, Hessenberger M, Puehringer S, Daumke O & Goettig P (2013) Functional mapping of human dynamin-1-like GTPase domain based on x-ray structure analyses. *PLoS One* 8

Whitley BN, Lam C, Cui H, Haude K, Bai R, Escobar L, Hamilton A, Brady L, Tarnopolsky MA, Dengle L, *et al* (2018) Aberrant Drp1-mediated mitochondrial division presents in humans with variable outcomes. *Hum Mol Genet* 27: 3710–3719

Wickham H (2016) ggplot2: Elegant Graphics for Data Analysis Springer-Verlag New York

Wickham H (2017) tidyverse: Easily Install and Load “Tidyverse” Packages. R package version 1.2.1.

Wickham H & Brian J (2019) readxl: Read Excel Files (Version 1.3.1). R package version 1.3.1. https://cran.r-project.or (https://cran.r-project.org/package=readxl) [PREPRINT]

Yamano K, Fogel AI, Wang C, van der Bliek AM & Youle RJ (2014) Mitochondrial Rab GAPs govern autophagosome biogenesis during mitophagy. *Elife* 3: 1–24

Yoon G, Malam Z, Paton T, Marshall CR, Hyatt E, Ivakine Z, Scherer SW, Lee KS, Hawkins C & Cohn RD (2016) Lethal Disorder of Mitochondrial Fission Caused by Mutations in DNM1L. *J Pediatr* 171: 313-316.e2

Yoon Y, Krueger EW, Oswald BJ & McNiven MA (2003) The mitochondrial protein {hFis1} regulates mitochondrial fission in mammalian cells through an interaction with the dynamin-like protein {DLP1}. *Mol Cell Biol* 23: 5409–5420

Zaha K, Matsumoto H, Itoh M, Saitsu H, Kato K, Kato M, Ogata S, Murayama K, Kishita Y, Mizuno Y, *et al* (2016) DNM1L -related encephalopathy in infancy with Leigh syndrome-like phenotype and suppression-burst. *Clin Genet* 90: 472–474

Zhang P & Hinshaw JE (2001) Three-dimensional reconstruction of dynamin in the constricted state. *Nat Cell Biol 2001 310* 3: 922–926

Zhu PP, Patterson A, Stadler J, Seeburg DP, Sheng M & Blackstone C (2004) Intra- and Intermolecular Domain Interactions of the C-terminal GTPase Effector Domain of the Multimeric Dynamin-like GTPase Drp1. *J Biol Chem* 279: 35967–35974

Figure Legends

Figure 1. Identification of five individuals harbouring *de novo* pathogenic variants in *DNM1L*.

(A) Family pedigrees of *DNM1L* patients. Affected individuals are shown in black, squares represent males, circles represent females, triangles represent pregnancy not carried to term and a diagonal line through the symbols indicate deceased subjects. **(B)** Schematic representation of known DRP1 variants and DRP1 protein domain organisation: BSE (bundle signalling element), GTPase domain, Stalk domain, Variable domain (VD) and the GTPase effector domain (GED). Variants identified in this study are shown in black and previously reported variants are in grey. Partial amino acid sequence alignments of DRP1 showing evolutionary conservation across different species.

Figure 2. *In silico* structural studies of *DNM1L* variants.

(A) Locations of pathologic variants marked on the crystal structure of nucleotide-free DRP1 (PDB: 4BEJ). **(B-D)** Residue-residue interactions and spatial relationships of residues to neighbouring motifs or DRP1 monomers of the wild type version of residues from A (CryoEM structure of DRP1 assembled and in complex with MID49, PDB: 5WP9). **(B)** Both G363 and G401 are alpha-helix capping residues found in close-proximity to each other between neighbouring DRP1 monomers. Substitution of either glycine to a charged aspartate (G363D) or polar serine (G401S) would induce unfavourable steric clashes with neighbouring residues and disrupt helix stability. **(C)** L230 is located within a small alpha helix between the G4 and G5 loop motifs, critical for nucleotide binding. Addition of another leucine to this helix may disrupt these motifs, impairing GTP binding. **(D)** The helix containing L230 is adjacent to the MID49 binding surface and the L230 duplication in this location may have negative effects on MID49 binding and recruitment of DRP1 to the mitochondria. **(E)** The residue R710G, located within the BSE domain, forms a salt bridge with E702. The R710G substitution would induce a loss of this salt bridge.

Figure 3. The impact of *DNM1L* variants on mitochondrial network length and DRP1 mitochondrial co-localisation.

(A) Representative images of TMRM stained mitochondrial network in paediatric (C1 and C2) and adult (C3 and C4) controls and *DNM1L* patient (P1-P4) fibroblasts. **(B)** Quantification of mean mitochondrial network length via MiNa using ImageJ n > 20 fields from two independent experiments, calculated by multiplying mean branch length and mean number of branches per network. Non-parametric one-way ANOVA and Dunn's multiple comparisons using GraphPad Prism were used to calculate statistically significant differences between groups. **(C)** Mitochondrial network length using immunofluorescence analysis of fixed paediatric control (C1), adult control (C2) and *DNM1L* patient (P1-P4) fibroblasts labelled with TOM20 antibodies. The Columbus (Perkin Elmer) software was used to quantify the hyperfusion of patient mitochondrial networks relative to controls and a minimum of 5,500 mitochondria were analysed for each case. The immunofluorescence labelling was performed three times. **(D)** Analysis of DRP1 co-localisation with the outer mitochondrial membrane protein TOM20 by immunofluorescence labelling of age-matched controls (C1 - paediatric, C2 - adult) and *DNM1L* patient (P1-P4) fibroblasts with anti-DRP1 (blue puncta) and anti-TOM20 (in red). DRP1 co-localisation with mitochondria was analysed in at least 32 cells per subject in two independent experimental sets. Pearson's correlations between DRP1 puncta and TOM20 in each cell line are shown as box plots. One-way ANOVA with post-hoc Tukey's Honest Significant Difference test was used to determine statistically significant differences (***P $\leq$ 0.001). Representative merged immunofluorescence images of fibroblasts stained with anti-TOM20 and anti-DRP1 antibodies are shown on the left.

Figure 4. The effect of *DNM1L* variants on peroxisomal morphology and co-localisation of DRP1 with peroxisomes.

(A) Analysis of peroxisome length by immunofluorescence using a peroxisomal membrane marker (PMP70) in fixed age-matched controls (C1 - paediatric, C2 - adult) and *DNM1L* patient (P1-P4) fibroblasts. The Columbus (Perkin Elmer) software was used to quantify the peroxisome length between patients and controls. The immunofluorescence labelling was performed three times and a minimum of 300 peroxisomes were analysed in each case. Statistically significant differences between groups were determined by a non-parametric one-way ANOVA (***P $\leq$ 0.001). Representative images of fixed cells stained for peroxisomes (PMP70) in control (C1, C2) and *DNM1L* patient (P1-P4) fibroblasts are shown on the left. **(B)** Immunofluorescence analysis of DRP1 puncta (blue) co-localising with

peroxisomes (PMP70 in red) in age-matched control (C1 - paediatric, C2 - adult) and *DNM1L* patient (P1-P4) fibroblasts. The analysis was performed on at least 32 cells from two independent experimental sets and mean values showing Pearson's correlation between the proportion of DRP1 puncta and peroxisomal marker PMP70 are shown. Statistically significant differences were calculated via a one-way ANOVA with post-hoc Tukey's Honest Significant Difference test (***P ≤ 0.001). Representative merged immunofluorescence images of PMP70 and DRP1 stained cells are shown on the left.

Figure 5. Clinically identified *DNM1L* variants alter GTPase activity.

(A) Substrate kinetics of recombinant wild type DRP1 (WT) (1 μM) and genetic variants. DRP1 GTPase activity was measured using an enzyme coupled assay monitoring NADH depletion, which is subsequently converted to activity (min^{-1}). Data from three independent experiments were globally fit to a Michaelis–Menten model. Residuals of the fit are shown. **(B)** Distribution of $K_{0.5}$, **(C)** k_{cat}, and **(D)** $k_{cat}/K_{0.5}$ parameters from GTPase activity measurements. Reported values were obtained by globally fitting DRP1 GTPase activity measurements (n = 3) to a Michaelis–Menten model. The resulting values are reported in Table 2. $K_{0.5}$ differences between WT and each variant significant to ***P<0.05. k_{cat} differences between WT and G363D, G363D and R710G, G363D and G401S, and R710G and G401S significant to ***P<0.05.

Figure 6. Patient DRP1 variants alter DRP1 assembly-state and melting temperature.

(A) SEC-MALS analysis of WT DRP1 (purple trace), DRP1 G363D (green trace), DRP1 G401S (orange trace), and DRP1 R710G (magenta trace) to assess for differences in multimeric distributions. Overlay of normalized differential refractive index of all protein samples (200 μg, 2.0 mg/mL) with peaks corresponding to monomeric, dimeric, and tetrameric oligomer species labeled as determined by predicted molecular masses of each multimeric species. Data normalized and scaled to allow for easier comparison due to slight differences in amount of protein loaded onto the column. **(B)** Melt curves of WT DRP1 and patient variants. Thermafluor analysis of protein unfolding of WT DRP1 (5.0 μM) and three patient variants (G363D, G401S, and R710G) either alone (black, dotted line), in the presence of 500 μM GDP (dark grey, dashed line), or GMP-PNP (light grey, solid line). **(C, D)** T_m values determined from the temperature corresponding to the maximum fluorescence

value in the absence of and presence of 500 μM GDP (dark grey) or GMP-PNP (light grey). Data plotted as the first derivative of the fluorescence signal with respect to time. C. Thermafluor analysis of the first protein unfolding event reported as the melting temperature (T_m) of WT DRP1 (5.0 μM) and three patient variants either alone, or in the presence of 500 μM GDP or GMP-PNP. D. Thermafluor analysis of the second protein unfolding event as value of the first derivative of the fluorescence signal. Only WT and R710G shown as they are the only two constructs with a prominent second unfolding event. Data is representative of two independent experiments, each with three technical replicates. *P<0.003, ***P<0.00001. Differences between T_m values of all constructs alone in comparison to constructs with 500 μM GDP or 500 μM GMP-PNP significant to P<0.003. T_m values of all constructs with 500 μM GDP in comparison to 500 μM GMP-PNP are significant to P<0.03 except for R710G with 500 μM GDP in comparison to R710G with 500 μM GMP-PNP where P<0.0003.

Supplementary Figure legends

Figure S1. Enlarged mitochondrial nucleoids identified in P1 and P2 *DNM1L* patient fibroblasts.

(A) Enlarged mitochondrial nucleoids observed in P1 (p.Gly401Ser), P2 (p.Glys363Asp), P3 (p.Leu230dup) and P4 (p.Arg710Gly) *DNM1L* patient fibroblasts incubated with TMRM. Nucleoids are indicated by yellow arrows. **(B)** Representative merged images of paediatric control (C1 and C2) and P1 (p.Gly401Ser) and P2 (p.Gly363Asp) fibroblasts stained with TMRM (mitochondria, red) and PicoGreen (mtDNA, green). Arrows highlight enlarged mitochondria with accumulations of mitochondrial DNA nucleoids. **(C)** Analysis of mtDNA nucleoids stained with PicoGreen fluorescent dye in age-matched C1 (paediatric), C2 (adult) controls and *DNM1L* patient (P1-P3) fibroblasts. The proportion of enlarged nucleoids >1.5 μm^2 was calculated in the total nucleoid pool. The minimum number of cells analysed from a random field of view was n = 21 and the smallest number of nucleoids analysed was 3400 (n = 3). Statistical differences between groups were determined by One-way ANOVA test [*$P \leq 0.05$; $P > 0.05$ n.s. (not significant)]. **(D)** Representative images of adult control (C2) and *DNM1L* P4 (p.Arg710Gly) fibroblasts stained with PicoGreen dye. Yellow arrows show enlarged mitochondrial DNA nucleoids in P4 cells, which also present with increased accumulation of lipofuscin granules.

Figure S2. Steady-state levels of fission machinery proteins in *DNM1L* patient fibroblasts

Immunoblotting analysis of paediatric (C1, C2) and adult controls (C3, C4) and *DNM1L* P1 (p.Gly401Ser), P2 (p.Glys363Asp), P3 (p.Leu230dup) and P4 (p.Arg710Gly) patient fibroblasts showing the steady state levels of DRP1 and MID51 proteins. The nuclear-encoded SDHA (Complex II) and β-actin were used as loading controls. Data information: Representative blots of three independent SDS-PAGE experiments are shown. Densitometric quantification of western blots showing the mean % of relative band intensities between *DNM1L* patients (P1-P4) and control samples (SDHA – loading control, CP – paediatric control, CA – adult control). The error bars represent standard deviation (n = 3).

Figure S3. Diagnostic quadruple immunofluorescent assay showing complex I-immunodeficient muscle fibres in *DNM1L* P2.

Mitochondrial respiratory chain expression profile plot showing COXI, NDUFB8 and porin protein levels in single muscle fibres from P2 (p.Gly363Asp). Each dot represents an individual muscle fibre, colour-coded according to its mitochondrial mass (very low: blue; low: light blue; normal: beige; high: orange; very high: red). Thin black dashed lines indicate the standard deviation (SD) limits for the classification of fibres, lines next to the x and y axes indicate the levels of NDUFB8 and COXI, respectively (beige: normal; light beige: intermediate (+); light blue: intermediate (++); blue: deficient). Bold dashed lines indicate the mean expression level of normal fibres.

Figure S4. Diagnostic mitochondrial respiratory chain complex activities in *DNM1L* patients.

(A, B) Diagnostic mitochondrial respiratory complexes activities (complexes I-IV) measured in control and *DNM1L* patient P2 (p.Gly363Asp), P3* (age 13y), P3** (age 16y) (p.Leu230dup) and P4 (p.Arg710Gly) muscle **(A)**, and in control and P2 fibroblasts **(B).** Data information: Mitochondrial respiratory chain enzyme activities were normalised to the activity of the mitochondrial matrix enzyme, citrate synthase. Mean enzyme activities of control muscle (n = 25) or fibroblasts (n = 8) are set to 100%, and error bars represent standard deviation.

Figure S5. *DNM1L* patient fibroblasts demonstrate OXPHOS deficiencies.

Immunoblotting analysis of whole cell lysates from paediatric (C1, C2) and adult controls (C3, C4) and *DNM1L* P1 (p.Gly401Ser), P2 (p.Glys363Asp), P3 (p.Leu230dup) and P4 (p.Arg710Gly) fibroblasts showing a decrease in the levels of multiple OXPHOS subunits. The nuclear-encoded SDHA (Complex II) and GAPDH were used as loading controls. Data information: Representative blots of three independent SDS-PAGE experiments are shown and densitometric quantification of western blots are showing the mean % of relative band intensities between *DNM1L* patients (P1-P4) and control samples (GAPDH – loading control,

CP – paediatric control, CA – adult control). The error bars represent standard deviation (n = 3).

Figure S6. Recombinant DRP1 WT and variants are well-folded.

Circular dichroism analysis of the far UV spectra of 0.05 mg/ml WT Drp1 (purple trace), Drp1 G363D (green trace), Drp1 G401S (orange trace), and Drp1 R710G (magenta trace) collected at 25 °C, converted to mean residue ellipticity, and scaled at 260 nm to achieve a baseline of 0.

Figure S7. Analysis of DRP1 oligomers in *DNM1L* patient fibroblasts.

(A) Immunoblot analysis of total cell lysates isolated from age-matched control (C1, C2-peadiatric and C3, C4 - adult) and *DNM1L* patient (P1 (p.Gly401Ser), P2 (p.Glys363Asp), P3 (p.Leu230dup) and P4 (p.Arg710Gly)) fibroblasts treated with DMSO only (-BMH) or the cross-linking reagent (+BMH) showing DRP1 higher order oligomers, DRP1 dimers (**) and DRP1 monomers (*). **(B)** The immunoblot analysis was repeated in control (C4) and *DNM1L* P4 (p.Arg710Gly) fibroblasts showing DRP1 complexes and Ponceau staining as indicated above. In **(A)** and **(B)** equal amounts of total cell lysates (50µg) were separated on a gradient (3-8%) Tris acetate gel. Data information: The analysis for P1-P3 was performed once **(A)** and a representative Western blot for control and P4 (p.Arg710Gly) is shown in **(B)** with densitometric quantification of relative band intensities (%) for monomeric DRP1 between control and P4. SDHA (n = 3) and HSP60 (n = 2) were used as loading controls and the error bars represent standard deviation.

Table 1. Clinical, genetic and pathological findings in individuals with *DNM1L* variants

ID	*DNM1L* variants				Clinical features	Muscle biopsy and laboratory findings	
	cDNA (NM_012062.5) protein (NP_036192.2)	**Age-at-onset**	**Clinical course**	**Consanguinity; Country of origin**	**Clinical features and relevant biochemical findings**	**Diagnostic muscle biopsy findings**	**Diagnostic biochemical findings**
Patient 1[a] female	c.1201G>A, p.(Gly401Ser) *De novo* heterozygous	8m	Died, 10m	No; UK	Seizures, developmental delay, microcephaly, sudden deterioration in feeding and breathing, brain MRI normal, ECG and echocardiogram abnormal, end stage dilated cardiomyopathy with previous signs of hypertrophic cardiomyopathy, raised 3-MGA type IV, plasma lactate 7.0 mmol/L (normal range 0.7-2.1mmol/L)	Hyperfused and enlarged mitochondria, abnormal mitochondrial morphology with low cristae density on TEM	Low complex IV ratio of 0.010 (0.014-0.034) in muscle
Patient 2[a,b] female	c.1088G>A, p.(Gly363Asp) *De novo* heterozygous	Birth	Died, 13m	No; UK	Seizures, growth failure, developmental delay, failure to thrive, microcephaly, micrognathia, infantile spasms, hypotonia, brain MRI abnormal, electroencephalogram abnormal – hypsarrthythmia, echocardiogram showed mild left ventricular hypertrophy, CSF lactate 4.6-7.0 mmol/L (normal range 0.7-2.1mmol/L)	n.d.	Complex I-immunodeficient muscle fibres (IHC) and low complex I and II respiratory chain complex activities in muscle; low complex I activities in fibroblasts
Patient 3[c] female	c.687_689dupATT, p.(Leu230dup) *De novo* heterozygous	6y	Died, 20y	No; UK Caucasian	Learning difficulties, epilepsy, ataxia, dystonia, myoclonus and peripheral neuropathy, blood and CSF lactate normal, glucose concentrations normal, urine organic acid and plasma amino acid analysis normal	Muscle electron microscopy and skin histology were not conclusive, but mainly normal	Complexes I-IV normal in the 1st muscle biopsy. 2nd muscle biopsy 3 years later showed decreased complex I and IV activity
Patient 4[d] male	c.2128A>G, p.(Arg710Gly) *De novo* heterozygous	3y	Died, 17y	No; UK	Chronic inflammatory demyelinating polyneuropathy, extra-pyramidal movement disorder, epilepsy, optic atrophy, fatigue and episodic regression of developmental skills precipitated by infection	n.d.	Mitochondrial respiratory chain activities (complexes I-IV) in muscle normal
Patient 5[d] male	c.1201G>A, p.(Gly401Ser) *De novo* heterozygous	33m	Alive, 3y	No; UK Caucasian	Early onset epileptic encephalopathy, global developmental delay, hypotonia, nystagmus, dyskinesia, lactate and pyruvate concentrations in the CSF normal, plasma amino acids, urinary amino acids, organic acids and urine sialic acid normal	n.d.	n.d.

[a] investigated by trio whole exome sequencing; [b] investigated by mitochondrial gene panel; [c] investigated by 100,000 genome project; [d] investigated by WES, n.d. – not determined, IHC - Quadruple immunofluorescent assay, MRI – magnetic resonance imaging, ECG – electrocardiogram, 3-MGA - 3-methylglutaconic aciduria

Table 2. Reported kinetic values among DRP1 variants. Kinetic parameters ($K_{0.5}$, V_{max}, k_{cat} and $k_{cat}/K_{0.5}$) were computed for DRP1 WT and each clinical variant.

	$K_{0.5}$ ± SD (μM)	V_{max} ± SD (μM/min)	k_{cat} (min^{-1})	k_{cat} (min^{-1}) /$K_{0.5}$ (μM)
WT	201 ± 51	0.24 ± 0.01	0.24×10^{-6}	1.2×10^{-9}
G363D	79 ± 11	0.58 ± 0.02	0.58×10^{-6}	7.3×10^{-9}
G401S	55 ± 9	0.36 ± 0.011	0.36×10^{-6}	0.65×10^{-9}
R710G	96 ± 18	0.10 ± 0.004	0.10×10^{-6}	1.0×10^{-9}

Supplementary information

Novel *DNM1L* variants impair mitochondrial dynamics through divergent mechanisms.

Kelsey A. Nolden[1*], John M. Egner[1*], Jack J. Collier[2,3], Oliver M. Russell[2], Charlotte L. Alston[2,4], Megan C. Harwig[1], Michael E. Widlansky[5], Souphatta Sasorith[6], Inês A. Barbosa[7], Andrew G. L. Douglas[8,9], Julia Baptista[10,11], Mark Walker[12], Deirdre E. Donnelly[13], Andrew A. Morris[14], Hui Jeen Tan[15], Manju A. Kurian[16], Kathleen Gorman[17,18], Santosh Mordekar[19], Charu Deshpande[20], Rajib Samanta[21], Robert McFarland[2,4], R. Blake Hill[1], Robert W. Taylor[2,4] and Monika Oláhová[2]

1. Expanded View Results, Materials and Methods

1.1 Clinical case reports

Patient 1

Patient 1 (P1) (c.1201G>A, p.Gly401Ser), a female, was the first child of non-consanguineous parents. The mother has Factor V Leiden-associated thrombophilia and had suffered nine spontaneous early miscarriages. Labour was induced at 37 weeks gestation following concerns regarding intrauterine growth restriction and birth weight was 2.24kg (9^{th} centile). In early infancy she was troubled by feeding difficulties, gastro-oesophageal reflux, faltering growth and had a febrile seizure at 5 months. Ophthalmology assessment at five months of age showed jerky smooth pursuit eye movements but was within normal limits. There was concern regarding her development on account of hypotonia and delayed motor milestones. On developmental assessment at the age of 8 months, she was able to hold her head up but was unable to roll over completely from back to front, and she could only sit with support. She was non-dysmorphic with a head circumference of 41.5 cm (2^{nd}-9^{th} centile) and a weight of 6.4 kg at 8 months (2^{nd}-9^{th} centile), with a length measured at 6 months of 62.2 cm (2^{nd}-9^{th} centile). At the age of 10 months, she was admitted to hospital following a 3-month history of deterioration with reduced feeding, tiredness, rapid breathing, sweating and pallor. On admission she had sinus tachycardia and a lactate of 7.0 mmol/L (normal range 0.7-2.1 mmol/L). An echocardiogram revealed severe dilated cardiomyopathy with a dilated left ventricle and concentric left ventricular hypertrophy with a trabeculated appearance especially over the apex. The left ventricle showed severe impairment of systolic function (ejection fraction 36%) along with diastolic dysfunction (left ventricular end diastolic diameter 26 mm). Her condition and cardiac function deteriorated, and her treatment became palliative. She passed away shortly after, aged 10 months. P1 has an older maternal half-brother who has a history of non-verbal autism and febrile seizures. Immunology, microbiology and virology investigations did not identify any underlying cause for her cardiomyopathy. Urine organic acid analysis showed mild ketonuria and significant dicarboxylic aciduria consistent with a fasting ketosis and raised 3-methylglutaconic acid, consistent with 3-methylglutaconic aciduria type IV. Notably, these changes were only transiently evident during her acute illness. Bloodspot acylcarnitines showed an increase in C2-carnitine and C4-OH-carnitine consistent with a ketogenic response to metabolic stress. Brain magnetic resonance imaging (MRI) showed no definite features of

leukodystrophy or basal ganglia signal abnormality, although there was equivocal pallidal high signal and mild thinning of the corpus callosum.

Patient 2

Patient 2 (P2) (c.1088G>A, p.Gly363Asp) was the first child of non-consanguineous parents and there was no family history of note on either side. Antenatally, there were significant concerns about growth which prompted delivery by caesarean section at 34+4 weeks gestation. Her birth weight was 1660 g (2^{nd}-9^{th} centile) and head circumference was 31 cm (25^{th} centile). No resuscitation was required but she spent 4 weeks in the Special Care Baby Unit. At 17 weeks of age (corrected age 11 weeks) her weight was 3.89 kg (0.4^{th} centile) her height and head circumference were also on the 0.4^{th} centile. At 21 weeks (corrected age 15 weeks) she developed infantile spasms and was admitted to hospital where she had a respiratory arrest. She showed a slow response to steroids and adrenocorticotropic hormone (ACTH). Developmentally, there were concerns regarding vision and development, as she was not smiling, or fixing and following. On examination at 24 weeks, she had microcephaly, arched eyebrows with upslanting palpebral fissures, and micrognathia. She had increased tone, with clenched hands and adducted thumbs. Her condition deteriorated and she died at the age of 13 months. Investigations showed raised lactate in cerebrospinal fluid (CSF), 5.5 mmol/L (normal range 1.2-2.1 mmol/L), and plasma 4.6 mmol/L (normal range 0.7-2.1 mmol/L) rising to 7.0mmol/L after 24 hours. Brain MRI showed hypoplasia of the corpus callosum and mild benign external hydrocephalus. Electroencephalogram (EEG) indicated hypsarrthythmia and echocardiogram revealed mild left ventricular hypertrophy.

Patient 3

Patient 3 (P3) (c.687_689dupATT, p.Leu230dup) was born to healthy non-consanguineous parents. She has a healthy brother and a healthy, non-identical, twin sister. P3 first presented at 6 years of age with chronic ataxia and mild learning difficulties. P3 developed left sided chorea and at 11 years of age, she had 3 generalised tonic-clonic convulsions. EEG showed frequent multifocal spike and wave activity with fronto-central emphasis and she was started on levetiracetam. Between 12 and 16 years of age, she had several admissions with status epilepticus or epilepsia partialis continua, with clonus of the left side of her face and arm. Between these episodes, she had moderately frequent focal seizures, such as left-sided facial clonic twitching without loss of consciousness. Various combinations of anticonvulsants were tried, along with a modified MCT-based ketogenic diet and subsequently vagus nerve

stimulation. She developed nocturnal enuresis at 12 years of age, associated with an unstable bladder. Over the next 2 years, her gait deteriorated and she developed dysarthria. At 15 years, she required a keyboard or a scribe for writing. Over the next 2 years, she developed dysphagia requiring gastrostomy-feeding, a motor axonal neuropathy, pain in her right leg probably from increased tone with a fixed flexion contracture of her right knee. MRI showed myositis ossificans with oedema and pockets of fluid in the erector spinae, gluteal and thigh muscles. At 18 years of age, communication was limited, and she had dystonia and myoclonus. She died aged 20 years. She had mild microcephaly (head circumference between 0.4th & 2nd centiles). Cranial MRI was normal initially, but she subsequently showed cerebellar atrophy and mild atrophy of the cerebral hemispheres. There was persistent lymphopenia. Blood and CSF lactate concentrations were normal at 1.5 mmol/L (normal range 0.7-2.1 mmol/L) and 1.3 mmol/L (normal range 1.2-2.1 mmol/L), respectively, at 12 years of age, as were the glucose concentrations (5.6 and 4.2 mmol/L (normal range 4.0-7.0 mmol/L)). Urine organic acid and plasma amino acid analyses were also normal.

Patient 4

Patient 4 (P4) (c.2128A>G, p.Arg710Gly) was born to non-consanguineous parents and has a healthy older sibling. The mother has coeliac disease and there is no relevant family history. P4 was born at 35 weeks gestation by emergency caesarean section following a pregnancy that was complicated by gestational diabetes. He weighed 3.2 kg. He was hypoglycaemic and was admitted to the Neonatal Intensive Care Unit where a left-sided ptosis led to a diagnosis of a congenital Horner's syndrome. He did not require artificial ventilation and bottle fed satisfactorily. He made good progress with motor skills initially, sitting at 8 months, but did not walk independently until 3-years when he had an ataxic gait. MRI of the brain at 1 and 2 years of age were normal. His left-sided ptosis was surgically corrected at 4 years of age at a time when "cryptogenic" epilepsy was diagnosed. Around this time, bilateral optic atrophy was identified; this remained stable with little impact on functional vision. MRI of the brain at the age of 5 years had subtle abnormalities in the parasagittal region of both hemispheres, suggestive of ulegyria. An extrapyramidal movement disorder began in his legs at 7 years and slowly progressed to his upper limbs by the age of 9 years. Scoliosis repair at age 8 years was followed by a loss of independent mobility. A severe aspiration pneumonia at 9 years of age required intensive care support and following videofluoroscopic confirmation of dysphagia he had a PEG inserted. Later that year electromyography and nerve conduction studies showed a severe underlying sensory-motor peripheral neuropathy, along with findings

indicative of a superimposed demyelinating neuropathy. Regular (6 weekly) infusions of intravenous immunoglobulin were commenced with good effect and were continued for almost 4 years. Further spinal surgery at the age of 11 years was followed by marked functional deterioration and profound gut dysmotility to the point of intestinal failure requiring total parenteral nutrition, upon which he remained dependent, and latterly a requirement for opioid analgesia to manage abdominal pain. L-Dopa treatment had some positive impact on his dystonia, rigidity and involuntary movement. A clinical assessment at the age of 16 years revealed an occipitofrontal head circumference of 53.9 cm and a weight of 34.1 kg. Neurologically, he had no independent mobility and used an electric wheelchair. Both upper limbs were held in an adducted and flexed position at elbows and wrists. Fine motor skills were impaired, though he did manage to use phone and tablets. He had very restricted movements at knees and ankles bilaterally. Cognitively he remained good and communicated effectively. He had infrequent epileptic seizures with focal onset and secondary generalisation but did not take anticonvulsant medication. At the age of 17 years, he deteriorated over the course of several months with severe abdominal pain, increasingly frequent seizures and progressive encephalopathy. TPN was thought to be prolonging an intolerable life and, following discussion with the family and wider clinical team, was withdrawn 4 weeks prior to his death in a hospice.

Patient 5

Patient 5 (P5) (c.1201G>A, p.Gly401Ser) is the first child of non-consanguineous white European parents, who presented with early onset epileptic encephalopathy with two episodes of status epilepticus at the age of 2 years and 9 months. He was originally referred for global developmental delay with significant delay in motor skills, speech and to some extent intellectual skills. He presented with a prolonged convulsive seizure (status epilepticus), which was controlled with medication. He was intubated, ventilated, and transferred to ITU for further care. Detailed neurometabolic screening involving lactate and pyruvate in the cerebrospinal fluid and neuroimaging were all normal. He also presented with ongoing semirhythmic/variable intensity persistent twitching motion in his left upper limb. Initial hemiparetic posture involving both upper and lower limbs gradually improved and was resolved with only residual mild left upper limb monoparesis. He experienced regression of some of his developmental skills during his recovery and is now completely non-verbal. He was also quite lethargic and hypotonic with additional concerns regarding his swallowing that prompted referral for a gastrostomy. A year later, he had another episode of status

epilepticus. Following recovery from two different episodes of status epilepticus, he was left with a semirepetitive dyskinesogenic high frequency movement disorder of variable intensity involving the upper limbs and face predominantly. He has a history of horizontal nystagmus. Repeat MRI imaging on this occasion showed disease progression with new bilateral high T2 and low T1 signal in the olivary nuclei of the medulla in keeping with cystic degeneration. There is less well defined T2 hyperintensity in the left thalamus. Neurometabolic screen involving lactate and pyruvate concentrations in the CSF, anti-neuronal antibodies and anti-NMDAR antibodies, plasma amino acids, urinary amino acids, organic acids, urine sialic acid screening was essentially normal.

1.2 Western blot analysis

Whole cell lysates from fibroblasts were lysed for 20 minutes on ice in lysis buffer [50 mM Tris-HCl pH 7.5, 130 mM NaCl, 2 mM $MgCl_2$, 1 mM phenylmethanesulfonyl fluoride (PMSF), 1% Nonidet P-40 (v/v) and 1 × EDTA free protease inhibitor cocktail], denatured at 95°C for 5 minutes and separated by 12% SDS as previously described (Oláhová *et al.*, 2015). Following electrophoretic transfer of proteins to polyvinylidene difluoride (PVDF) membranes, immunoblotting was performed using antibodies against DRP1 (BD Transduction laboratories, 611113), Total OXPHOS Human WB Antibody Cocktail (Abcam, ab110411), SMCR7L (MID51) (ab89944), ß-actin (Cloud Clone Corp. CAB340Hu22) and GAPDH (Proteintech 60004-1-Ig).

For SDS-PAGE immunoblotting analysis, species appropriate horseradish peroxidase-conjugated secondary antibodies (Dako) were used and all the primary antibodies were diluted 1:1000 except for ß-actin (1:10 000) and GAPDH (1:2000). Amersham ECL Prime Western Blotting Detection Reagent (GE Healthcare, Life Sciences) and The Bio-Rad ChemiDoc MP with Image Lab software were used for protein visualisation and densitometry quantification of the blots.

1.3 BMH crosslinking

Control and patient (P4) primary fibroblasts were harvested at ~80% confluency, washed in 1x PBS and pellets were lysed in 200 µl lysis buffer [10 mM HEPES, 150 mM NaCl, 1 mM EGTA, 1% Triton-X (v/v), 1mM PMSF and 1 × EDTA free protease inhibitor cocktail] containing 1mM DMSO or 1mM bis-maleimido-hexane (BMH) cross-linker for 30 minutes at RT with gentle rotation. The reaction was inactivated by the addition of 20 mM DTT for 15 minutes at RT. Protein concentration of the supernatant following centrifugation

of the lysates at 500 rcf for 5 minutes was determined by Bradford assay (BioRad) and 50 µg of each sample, denatured at 70°C for 10 minutes in the presence of NuPAGE™ LDS Sample Buffer (ThermoFisher), was loaded onto a NuPAGE 3-8% Tris Acetate Gel (Novex) and analysed by Western blotting.

References

Oláhová M, Hardy SA, Hall J, Yarham JW, Haack TB, Wilson WC, Alston CL, He L, Aznauryan E, Brown RM, et al (2015) *LRPPRC* mutations cause early-onset multisystem mitochondrial disease outside of the French-Canadian population. Brain 138: 3503–3519

Figure 1

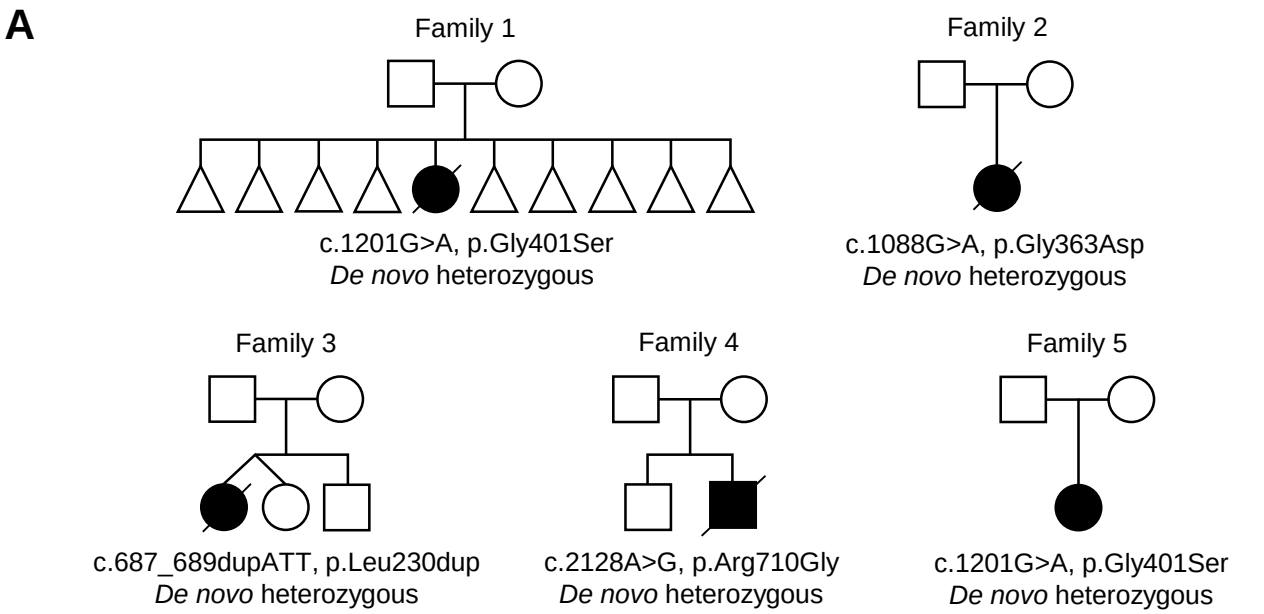
A
Family 1
c.1201G>A, p.Gly401Ser
De novo heterozygous
Family 2
c.1088G>A, p.Gly363Asp
De novo heterozygous
Family 3
c.687_689dupATT, p.Leu230dup
De novo heterozygous
Family 4
c.2128A>G, p.Arg710Gly
De novo heterozygous
Family 5
c.1201G>A, p.Gly401Ser
De novo heterozygous

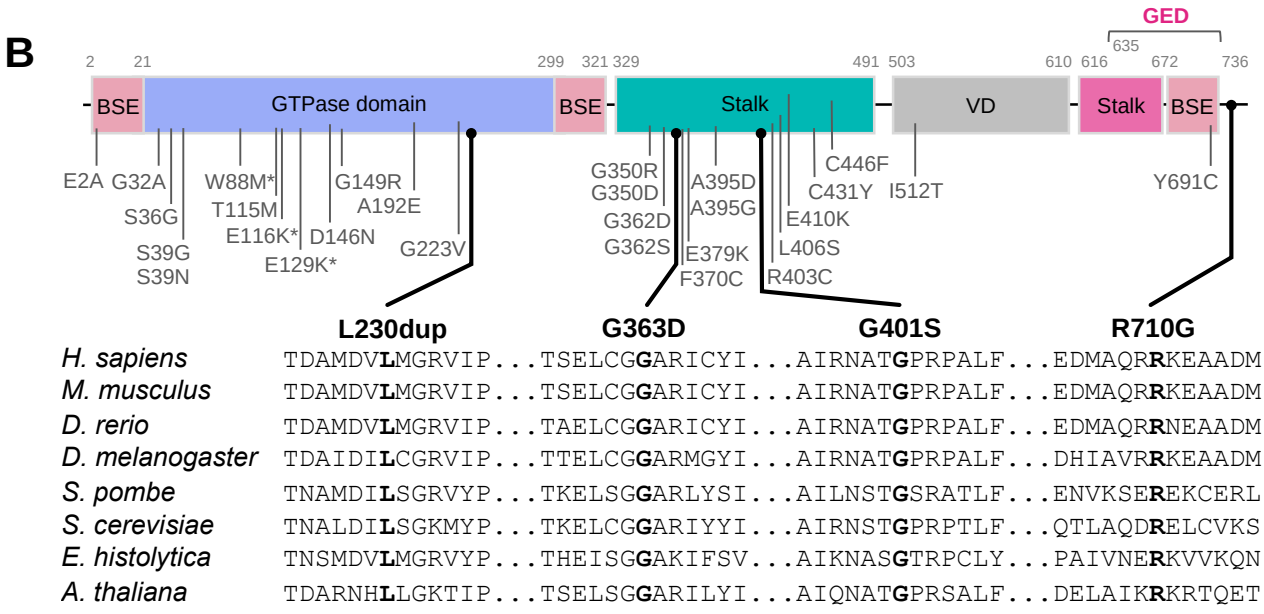
B
GED
2 21 299 321 329 491 503 610 616 635 672 736
BSE
GTPase domain
BSE
Stalk
VD
Stalk
BSE
E2A G32A S36G S39G S39N
W88M* T115M E116K* E129K* D146N
G149R A192E
G223V
G350R G350D G362D G362S
A395D A395G E379K F370C
E410K L406S R403C
C446F C431Y
I512T
Y691C
L230dup
G363D
G401S
R710G
H. sapiens TDAMDVLMGRVIP...TSELCGGARICYI...AIRNATGPRPALF...EDMAQRRKEAADM
M. musculus TDAMDVLMGRVIP...TSELCGGARICYI...AIRNATGPRPALF...EDMAQRRKEAADM
D. rerio TDAMDVLMGRVIP...TAELCGGARICYI...AIRNATGPRPALF...EDMAQRRNEAADM
D. melanogaster TDAIDILCGRVIP...TTELCGGARMGYI...AIRNATGPRPALF...DHIAVRRKEAADM
S. pombe TNAMDILSGRVYP...TKELSGGARLYSI...AILNSTGSRATLF...ENVKSERKCERL
S. cerevisiae TNALDILSGKMYP...TKELCGGARIYYI...AIRNSTGPRPTLF...QTLAQDRELCVKS
E. histolytica TNSMDVLMGRVYP...THEISGGAKIFSV...AIKNASGTRPCLY...PAIVNERKVVKQN
A. thaliana TDARNHLLGKTIP...TSELSGGARILYI...AIQNATGPRSALF...DELAIKRKRTQET

Figure 2

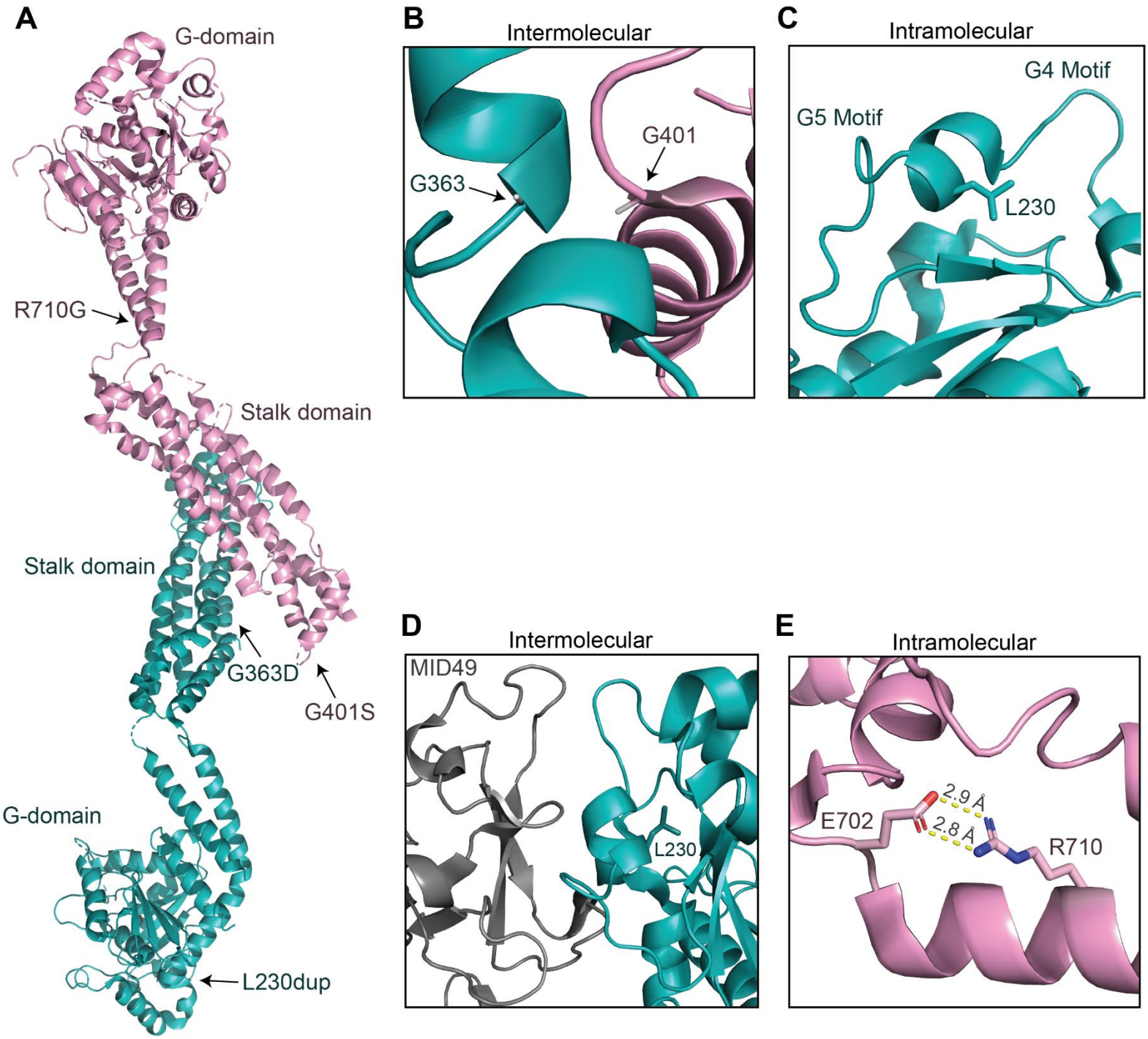
A
G-domain
R710G
Stalk domain
Stalk domain
G363D
G401S
G-domain
L230dup
B
Intermolecular
G401
G363
C
Intramolecular
G4 Motif
G5 Motif
L230
D
Intermolecular
MID49
L230
E
Intramolecular
2.9 Å
2.8 Å
E702
R710

Figure 3

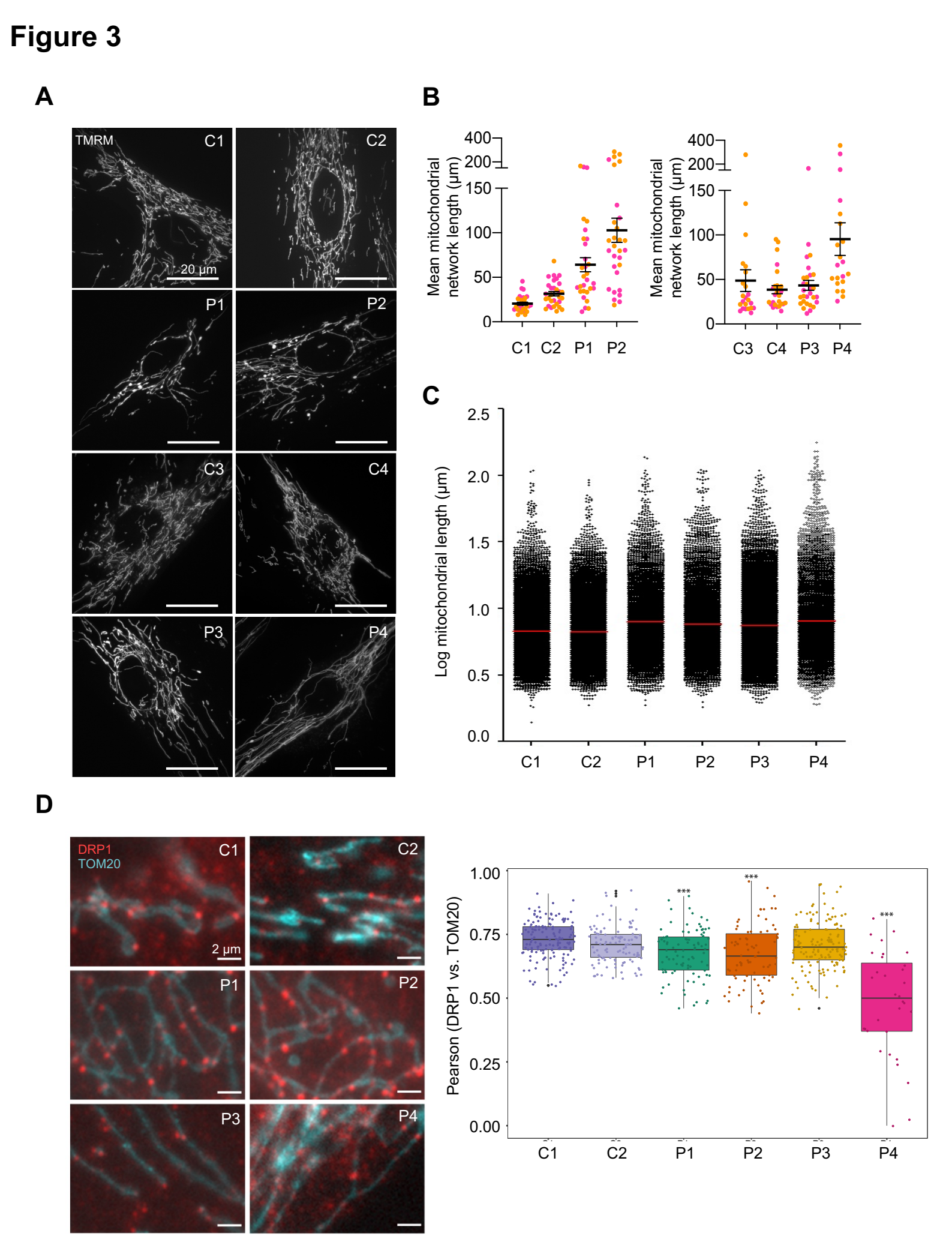
A
TMRM
C1
C2
20 µm
P1
P2
C3
C4
P3
P4
B
Mean mitochondrial network length (µm)
400
200
150
100
50
0
C1 C2 P1 P2
C3 C4 P3 P4
C
Log mitochondrial length (µm)
2.5
2.0
1.5
1.0
0.5
0.0
C1 C2 P1 P2 P3 P4
D
DRP1
TOM20
C1
C2
2 µm
P1
P2
P3
P4
Pearson (DRP1 vs. TOM20)
1.00
0.75
0.50
0.25
0.00
***
C1 C2 P1 P2 P3 P4

Figure 4

A

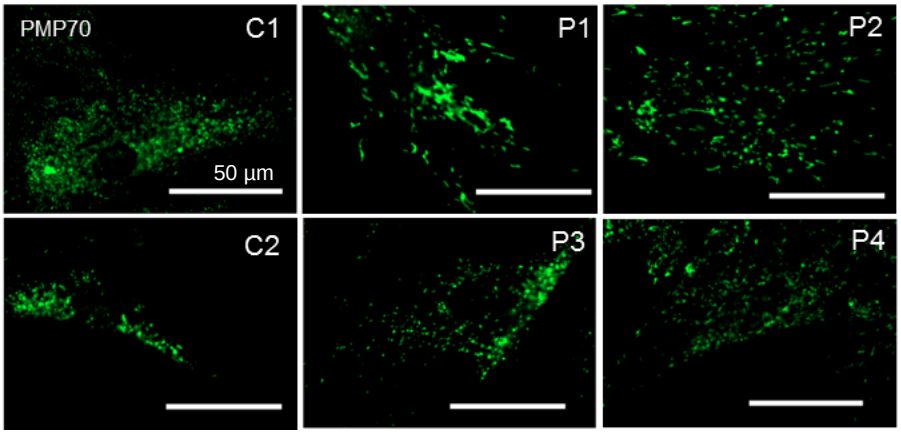
PMP70
C1
50 µm
P1
P2
C2
P3
P4

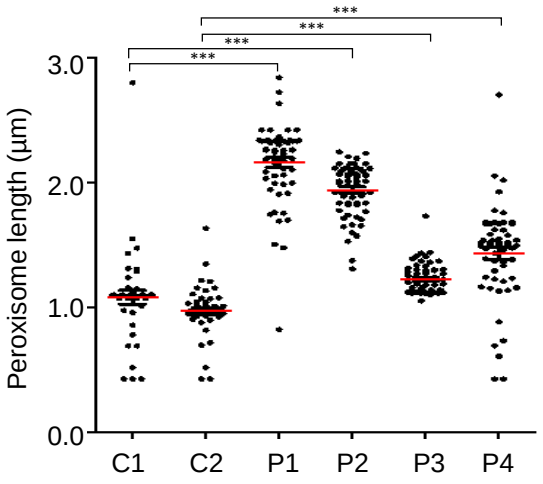
***
***
***
***
Peroxisome length (µm)
3.0
2.0
1.0
0.0
C1
C2
P1
P2
P3
P4

B

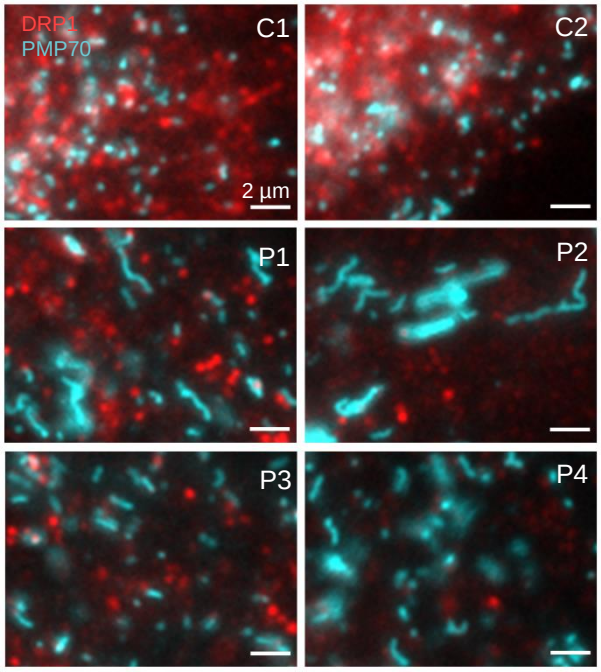
DRP1
PMP70
C1
2 µm
C2
P1
P2
P3
P4

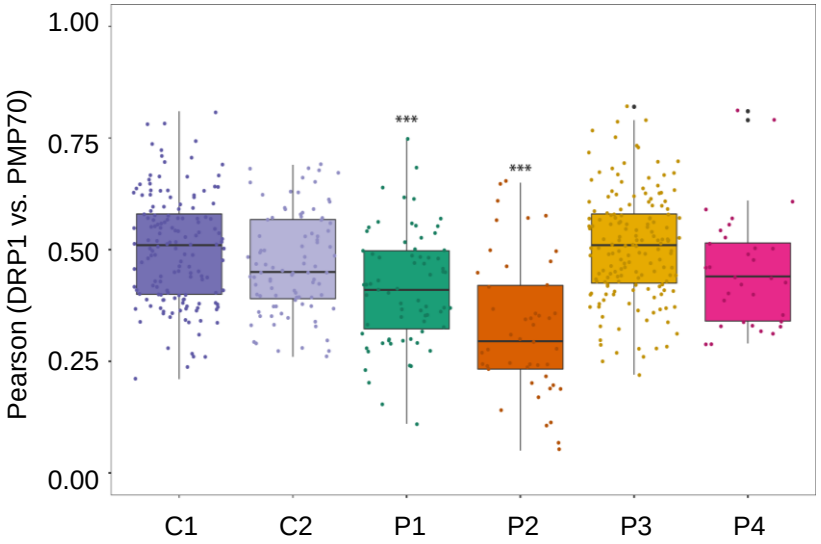
Pearson (DRP1 vs. PMP70)
1.00
0.75
0.50
0.25
0.00
***
***
C1
C2
P1
P2
P3
P4

Figure 5

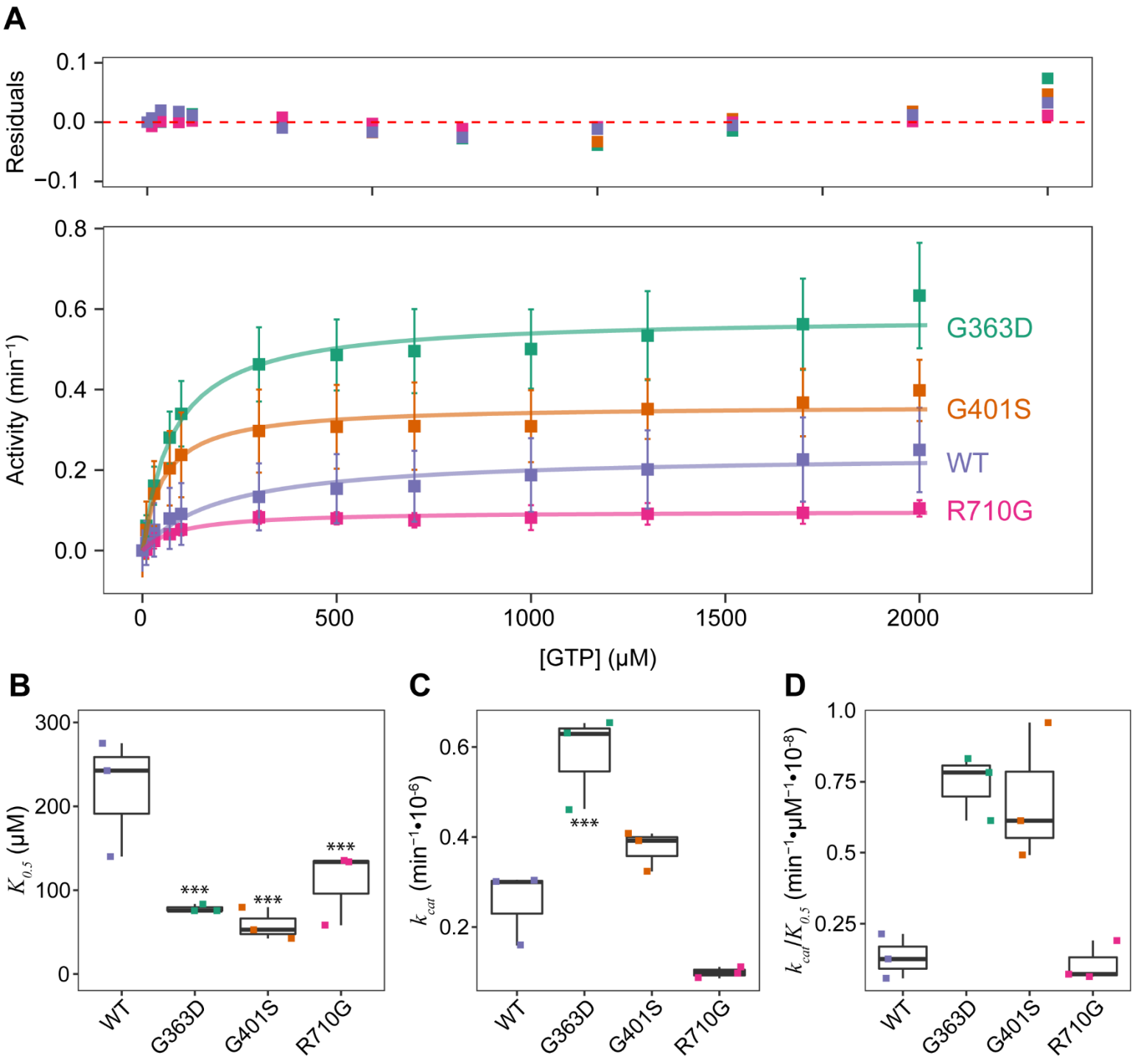
A
Residuals
0.1
0.0
−0.1
Activity (min⁻¹)
0.8
0.6
0.4
0.2
0.0
0
500
1000
1500
2000
[GTP] (μM)
G363D
G401S
WT
R710G
B
$K_{0.5}$ (μM)
300
200
100
0
***
***
***
WT
G363D
G401S
R710G
C
k_{cat} (min⁻¹•10⁻⁶)
0.6
0.4
0.2
***
WT
G363D
G401S
R710G
D
$k_{cat}/K_{0.5}$ (min⁻¹•μM⁻¹•10⁻⁸)
1.0
0.75
0.5
0.25
WT
G363D
G401S
R710G

Figure 6

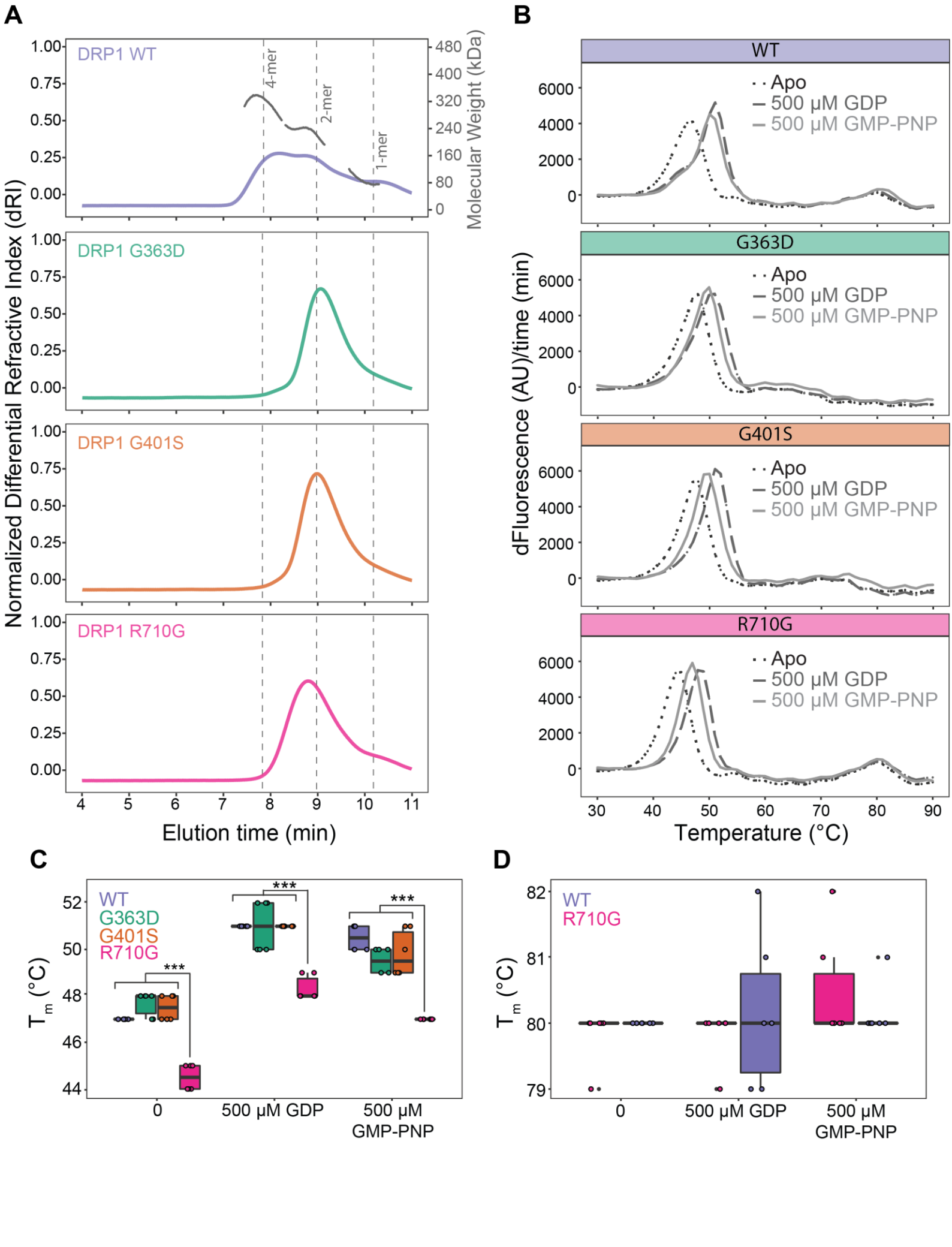
A
DRP1 WT
DRP1 G363D
DRP1 G401S
DRP1 R710G
4-mer
2-mer
1-mer
Normalized Differential Refractive Index (dRI)
Molecular Weight (kDa)
Elution time (min)
B
WT
G363D
G401S
R710G
Apo
500 µM GDP
500 µM GMP-PNP
dFluorescence (AU)/time (min)
Temperature (°C)
C
WT
G363D
G401S
R710G
T_m (°C)
***
0
500 µM GDP
500 µM GMP-PNP
D
WT
R710G
T_m (°C)
0
500 µM GDP
500 µM GMP-PNP

Figure S1

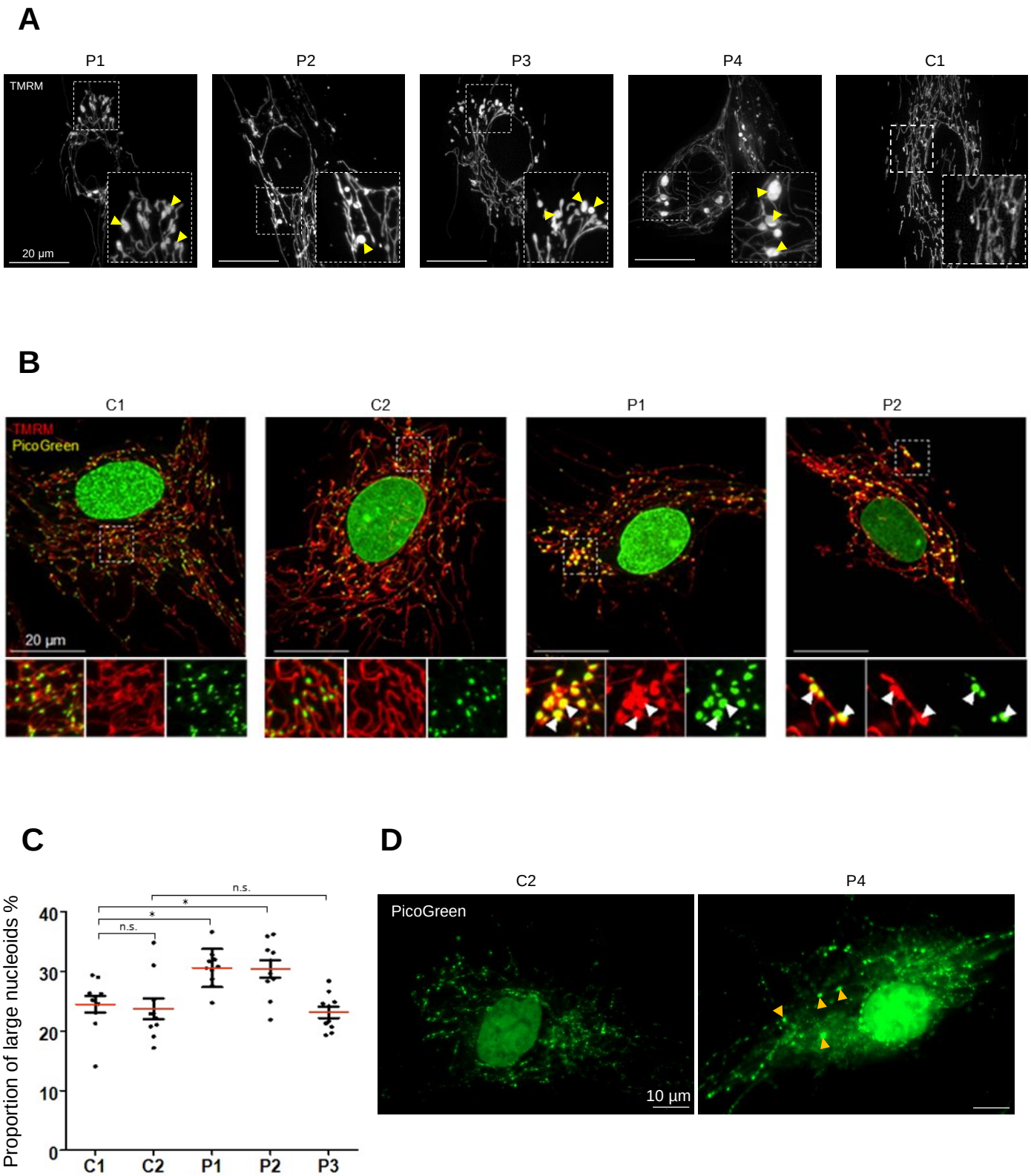
A
P1
P2
P3
P4
C1
TMRM
20 µm
B
C1
C2
P1
P2
TMRM
PicoGreen
20 µm
C
Proportion of large nucleoids %
40
30
20
10
0
n.s.
*
*
n.s.
C1
C2
P1
P2
P3
D
C2
P4
PicoGreen
10 µm

Figure S2

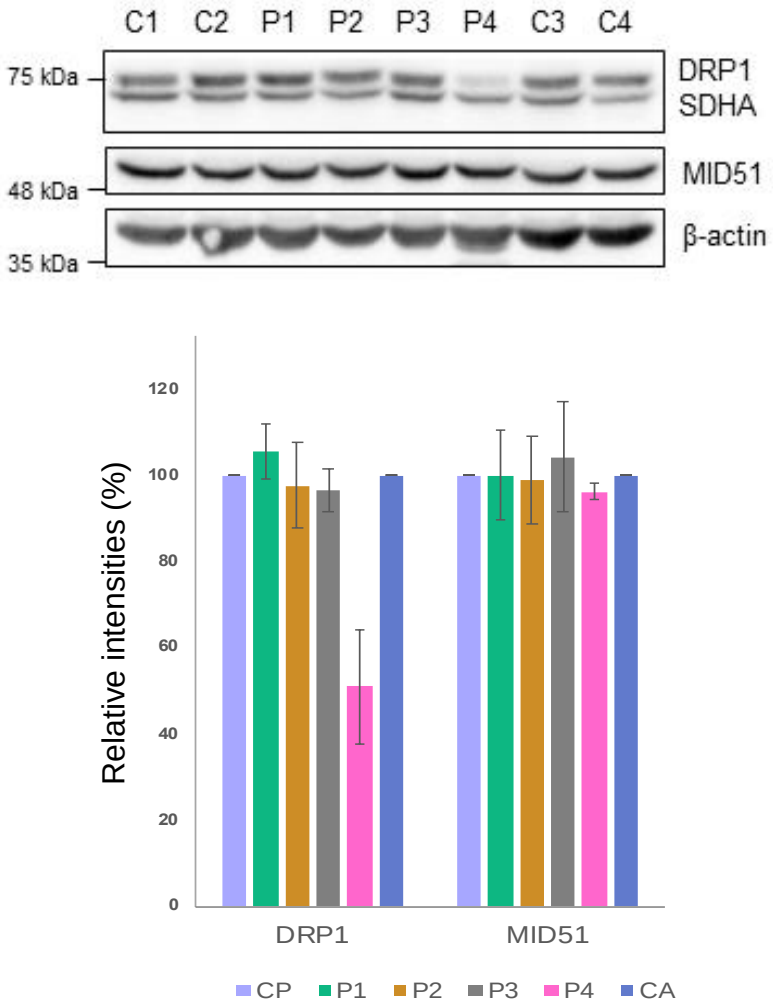
C1
C2
P1
P2
P3
P4
C3
C4
75 kDa
48 kDa
35 kDa
DRP1
SDHA
MID51
β-actin
Relative intensities (%)
120
100
80
60
40
20
0
DRP1
MID51
CP
P1
P2
P3
P4
CA

Figure S3

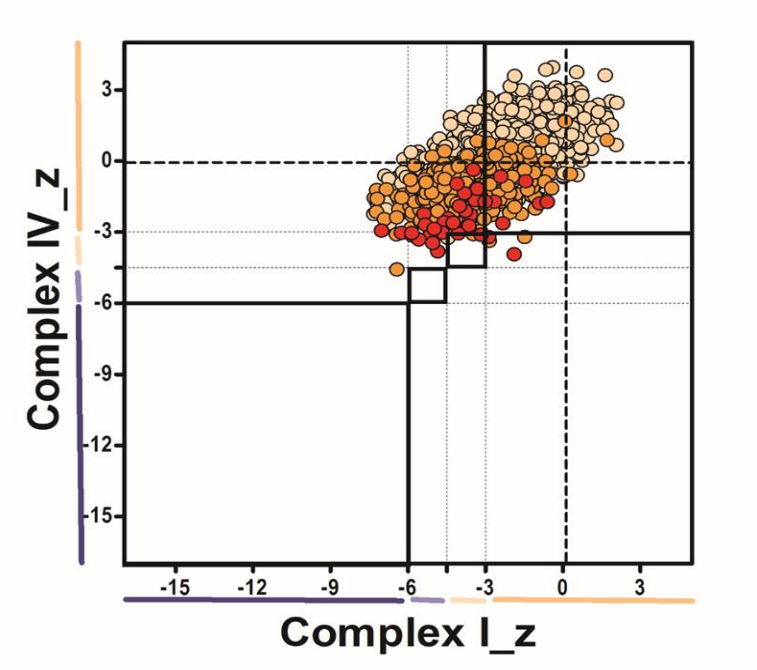

Figure S4

A

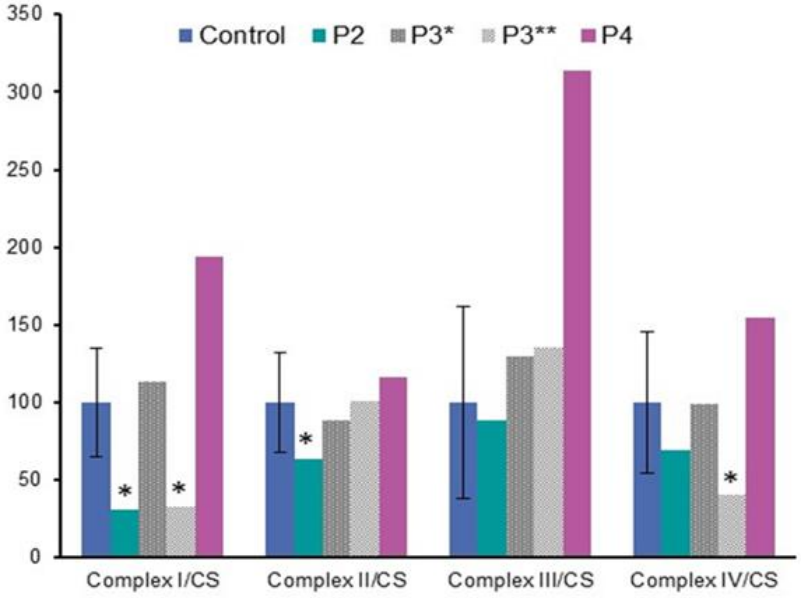
Control
P2
P3*
P3**
P4
350
300
250
200
150
100
50
0
*
*
*
Complex I/CS
Complex II/CS
Complex III/CS
Complex IV/CS

B

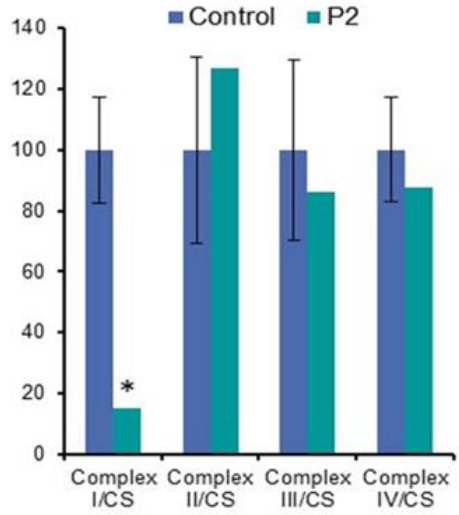
Control
P2
140
120
100
80
60
40
20
0
*
Complex I/CS
Complex II/CS
Complex III/CS
Complex IV/CS

Figure S5

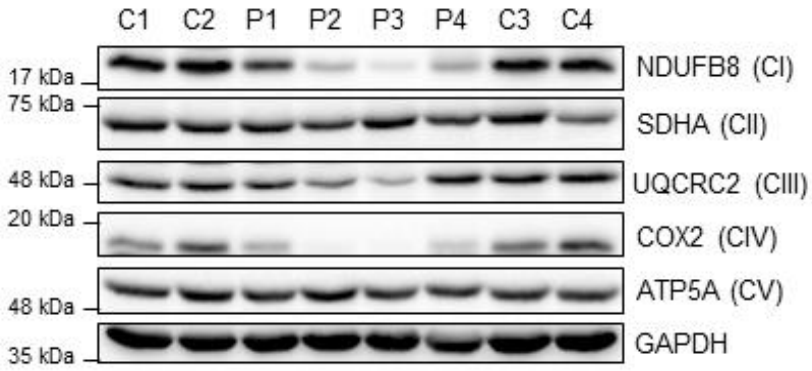
C1
C2
P1
P2
P3
P4
C3
C4
17 kDa
75 kDa
48 kDa
20 kDa
48 kDa
35 kDa
NDUFB8 (CI)
SDHA (CII)
UQCRC2 (CIII)
COX2 (CIV)
ATP5A (CV)
GAPDH

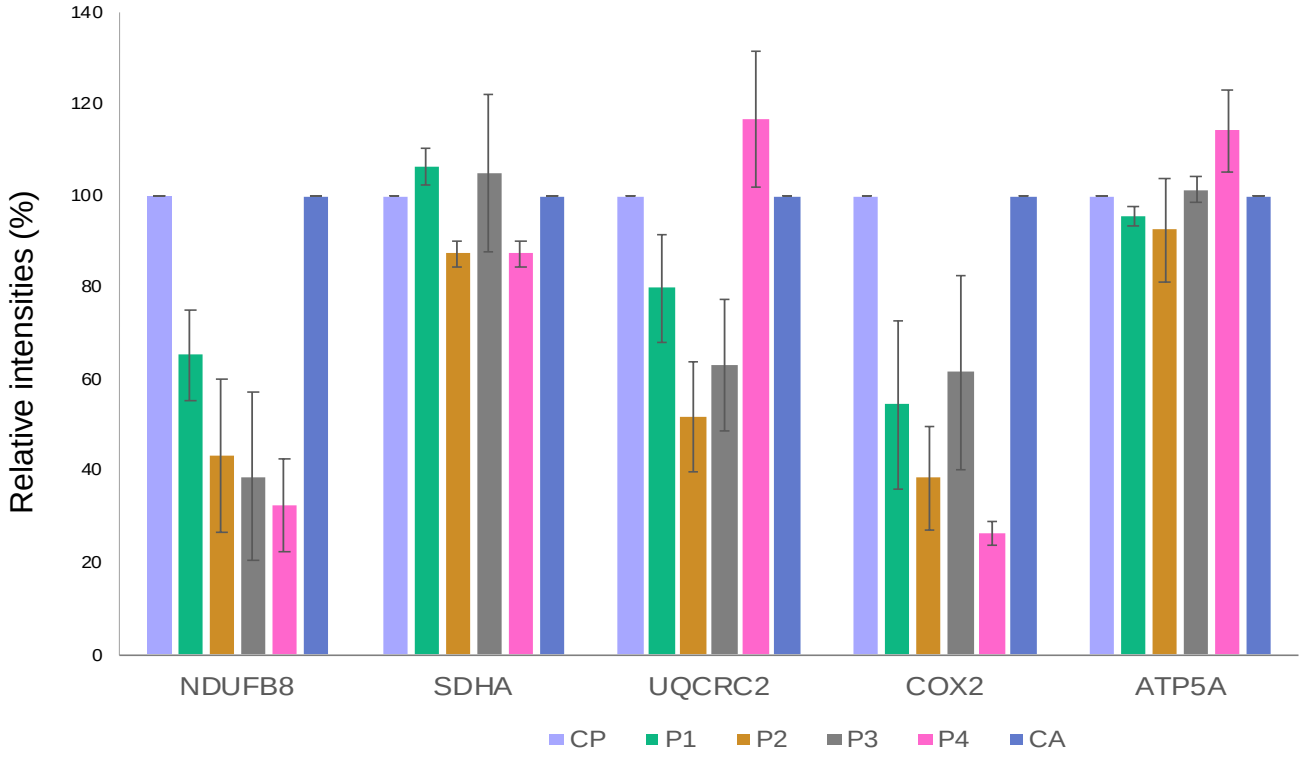
Relative intensities (%)
140
120
100
80
60
40
20
0
NDUFB8
SDHA
UQCRC2
COX2
ATP5A
CP
P1
P2
P3
P4
CA

Figure S6

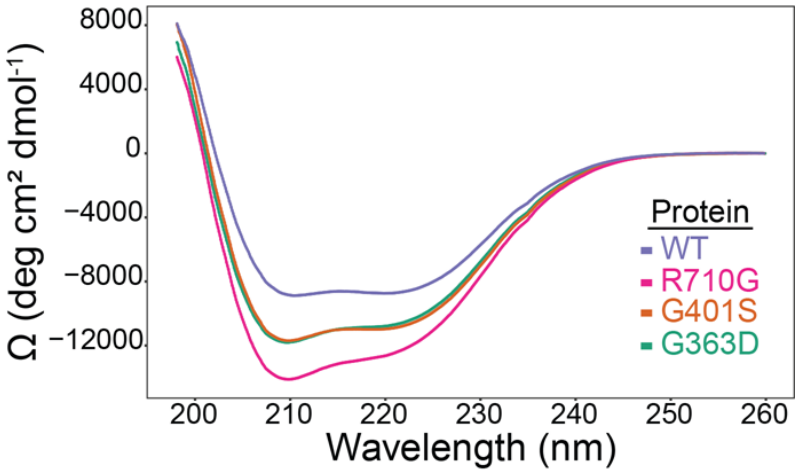
8000
4000
0
−4000
−8000
−12000
Ω (deg cm² dmol⁻¹)
200
210
220
230
240
250
260
Wavelength (nm)
Protein
WT
R710G
G401S
G363D

Figure S7

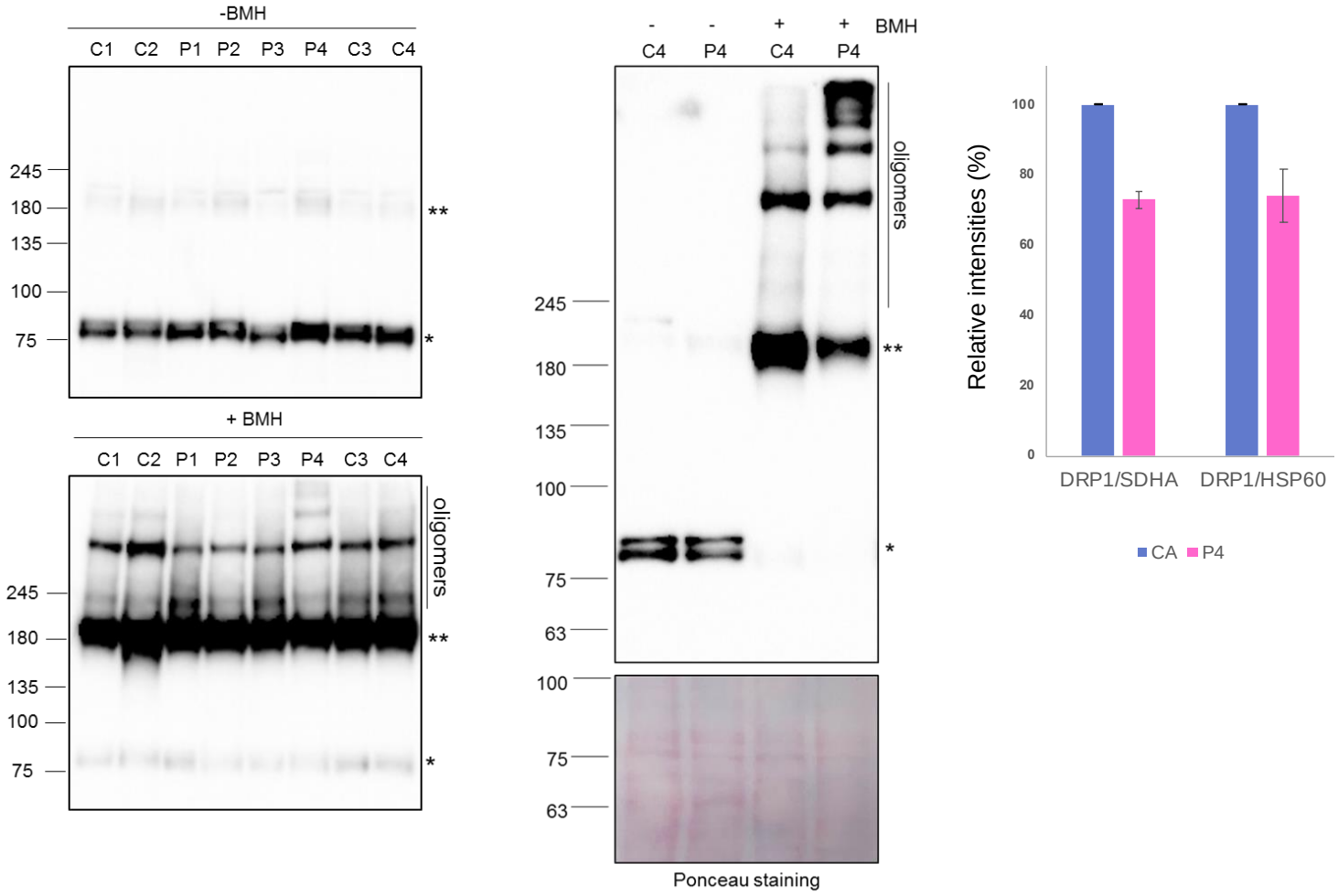
-BMH
C1 C2 P1 P2 P3 P4 C3 C4
245
180
135
100
75
**
*
+ BMH
C1 C2 P1 P2 P3 P4 C3 C4
oligomers
245
180
135
100
75
**
*
- - + + BMH
C4 P4 C4 P4
oligomers
245
180
135
100
75
63
**
*
100
75
63
Ponceau staining
Relative intensities (%)
100
80
60
40
20
0
DRP1/SDHA
DRP1/HSP60
CA
P4